UNIVERSITÀ
DI PAVIA

Dipartimento di Fisica

Corso di laurea magistrale in Scienze fisiche

Tissue-Specific Radiobiological Modeling for Space Radiation Risk Assessment

Modellizzazione radiobiologica tessuto-specifica per la valutazione del rischio da radiazioni spaziali

Tesi per la laurea di:

Beatrice Accotto

Supervisor:

Prof. Ricardo Luis Ramos

Co-Supervisors:

Prof. Francesca Ballarini

Prof. Mario Pietro Carante

Anno accademico 2025 – 2026

Abstract

Space radiation represents a critical constraint in space exploration; thus, investigating its impact on human tissues is essential for implementing shielding solutions and minimizing astronaut exposure. Indeed, as future space missions are expected to comprise increasingly diverse astronaut populations, including a growing number of female crew members, assessing gender specific health risks is of primary importance.

A major frontier in radiation protection research involves evaluating radiation effects across distinct cell types, and within this framework, this thesis contributes by determining the biophysical parameters for two cell lines, HaCaT (keratinocyte) and MCF10A (mammary epithelial cell line), and refining them for fibroblasts (HSF) under ion irradiation at different Linear Energy Transfer (LET) values. This collection of parameters constitutes the radiobiological database developed in this work. Experimental cell survival data were analyzed using the BIANCA biophysical model to calibrate the model itself and generate the databases.

Since the HaCaT and MCF10A cell lines are representative of skin and breast tissues, respectively, this work focuses on these two targets. This is highly advantageous as the skin is the primary organ exposed to space radiation, while the breast is a highly radiosensitive tissue of critical relevance for female astronauts.

The radiation source chosen is the August 1972 Solar Particle Event (SPE), selected for its extreme severity. To evaluate its biological effects, an interface between the FLUKA Monte Carlo radiation transport code and the BIANCA biophysical model was exploited, incorporating both the existing and the newly developed databases. The investigated configurations included male and female phantoms inside spherical and cylindrical spacescraft of various shielding thicknesses, assessing both absorbed dose and Relative Biological Effectiveness (RBE)-weighted absorbed dose.

Results showed that the new HaCaT and MCF10A datasets exhibit greater radioresistance than the HSF database. Regarding spacecraft geometry, absorbed doses were systematically higher under spherical shielding than cylindrical configurations. Furthermore, for the August 1972 SPE, the new database yielded higher RBE-weighted doses at low shielding thicknesses, showing a relative difference of approximately 10% compared to the HSF baseline. Conversely, for larger shielding thicknesses, the HSF database becomes more conservative, exceeding the new values by about 10%.

Since SPEs typically unfold over several hours, evaluating the effects of a protracted dose is crucial. This time-dependent consideration was found to have a significantly higher impact under light shielding conditions, in more superficial organs, and when employing the fibroblast database. For instance, for the skin at 0.3 g/cm^2 using the HSF database, the relative difference between an acute exposure and a 16-hour protracted irradiation is approximately 35%.

Overall, this work provides the first BIANCA radiobiological databases for HaCaT and MCF10A cells and demonstrates that tissue-specific radiobiological characterization significantly improves radiation risk assessment for space applications.

Abstract in lingua italiana

Le radiazioni spaziali rappresentano un vincolo critico per l'esplorazione spaziale e studiare il loro impatto sui tessuti umani risulta essenziale per implementare soluzioni di schermatura adeguate e minimizzare l'esposizione degli equipaggi. Inoltre, poiché si prevede che le future missioni spaziali includeranno equipaggi sempre più diversificati, con un numero crescente di astronaute, valutare i rischi per la salute specifici di genere riveste un'importanza primaria.

Una delle principali frontiere nella ricerca in radioprotezione riguarda la valutazione degli effetti delle radiazioni in diversi tipi di cellule. Questa tesi contribuisce a tale scopo determinando i parametri biofisici per due linee cellulari, HaCaT (keratinociti) e MCF10A (linea cellulare epiteliale mammaria), e perfezionando quelli per i fibroblasti (HSF) sotto irradiazione da ioni a diversi valori di Linear Energy Transfer (LET). Questo set di parametri costituisce il database radiobiologico, generato calibrando il modello biofisico BIANCA su dati sperimentali di sopravvivenza cellulare. Il lavoro si concentra su pelle e seno, rappresentati rispettivamente dalle linee HaCaT e MCF10A e ciò risulta estremamente vantaggioso in quanto la pelle è il principale organo esposto alle radiazioni, mentre il seno è un tessuto altamente radiosensibile e critico per le astronaute.

Come sorgente è stato scelto l'Evento di Particelle Solari (SPE) dell'agosto 1972, selezionato per la sua estrema intensità. Per valutarne gli effetti biologici, è stata utilizzata un'interfaccia tra il codice di trasporto Monte Carlo FLUKA e il modello biofisico BIANCA, incorporando sia il database preesistente sia quelli sviluppati nella tesi. Si sono simulati fantocci maschili e femminili all'interno di veicoli spaziali con forma sferica e cilindrica di vari spessori di schermatura, valutando sia la dose assorbita, sia la dose assorbita pesata sull'Effetto Biologico Relativo (RBE).

I risultati hanno mostrato che i dataset per HaCaT e MCF10A presentano una maggiore radioresistenza rispetto a HSF; per quanto riguarda la geometria dei veicoli spaziali, le dosi assorbite sono risultate sistematicamente superiori nella configurazione sferica rispetto a quella cilindrica. Inoltre, per l'SPE dell'agosto 1972, a bassi spessori di schermatura, il nuovo database HaCaT-MCF10A ha fornito dosi pesate sull'RBE superiori di circa il 10% rispetto a HSF; al contrario, a spessori maggiori, il database HSF è risultato più conservativo di circa il 10%.

Poiché gli SPE tipicamente si sviluppano nell'arco di diverse ore, valutare gli effetti di una dose protratta nel tempo è cruciale. La valutazione temporale è risultata avere un impatto maggiore in condizioni di schermatura leggera, negli organi più superficiali e usando il database HSF. Per esempio, per la pelle a uno spessore di 0.3 g/cm^2 con il database HSF, la differenza relativa tra un'esposizione acuta e un'irradiazione protratta di 16 ore è circa il 35%.

In conclusione, questo lavoro fornisce i primi database radiobiologici BIANCA per le cellule HaCaT e MCF10A e dimostra che la caratterizzazione radiobiologica tessuto-specifica migliora significativamente la valutazione del rischio da radiazioni per le applicazioni spaziali.

Contents

CHAPTER 1

Introduction

Human crews face numerous health and performance hazards during space missions. According to NASA website [1], these include conditions such as venous thromboembolism, adverse host-microorganism interactions, and in-flight medical emergencies. These issues are directly linked to the primary hazards of spaceflight: elevated radiation levels, altered gravity fields, long periods of isolation, a closed living environment, and the stress of being far from Earth.
This work focuses specifically on exposure to ionizing radiation. It is classified as a "red risk," meaning it has the highest priority based on both its likelihood of occurrence and the severity of its impact on human health, in-mission performance, and long-term quality of life. Ultimately, radiation exposure represents the main limiting factor for long-duration missions [2] [3].

This chapter first outlines the sources of ionizing radiation in space, followed by the definitions of the quantities used to characterize the impact of particles on living matter, and an overview of the potential effects of radiation on astronaut health. Subsequently, radiation protection strategies for space missions, along with the limits imposed by space agencies, are presented, and the biological damage to cells and DNA is described. Finally, the necessity of a cell-specific radiobiological model capable of accounting for the variations in response across different cell lines, is highlighted.

1.1 Space radiation environment

In space missions, the three main contributions to be considered are protons and electrons trapped by the Earth's intrinsic magnetic field, Galactic Cosmic Rays (GCRs), and Solar Particle Events (SPEs) [4]. The first component, which is often neglected in long-term space missions, is briefly described below, prior to focusing on the remaining two, which constitute the primary sources of space radiation of concern for radiation protection.

Regarding trapped radiation, the Earth's magnetic field affects the free-space environment by both repelling low-energy ions and trapping charged particles (protons and electrons produced in the atmosphere) in the Van Allen belts [2] [5]. The particles in the Van Allen belts move in a spiral trajectory along the geomagnetic field lines and are reflected back between the magnetic poles. The maximum extent of these belts is located above the Equator, where they span from approximately 200 km out to 40 000–60 000 km above the Earth's surface [6]. The Van Allen belts are divided into two distinct regions: the inner belt and the outer belt. A difference between the two belts is their particle composition: the inner belt is mainly composed of protons with energies up to 500 MeV, whereas the outer belt consists predominantly of electrons with energies in the MeV range.
The intensity of trapped particles could be harmful due to the high particle fluxes and substantial potential doses; however, vehicles traverse this region quickly enough to ensure minimal exposure to astronauts and electronics. Consequently, this type of radiation is typically omitted in long-term mission planning [2] [4].

1.1.1 Galactic Cosmic rays (GCR)

Galactic Cosmic rays (GCR) originate outside the Solar System from supernova explosions, neutron stars, pulsars, or other sources involving high-energy phenomena [5]. They consist of a continuous and isotropic flux of high-energy ions spanning a broad range of atomic numbers. Due to these varying atomic numbers, evaluating each ion species requires measuring not only its fluence, but also its specific contribution to the dose and dose equivalent [1] . Their relative contributions are shown in Figure 1.1.
Concerning the GCR composition, they are composed by baryons (about 98%)

[1] Dose and dose equivalent are defined in Section 1.2

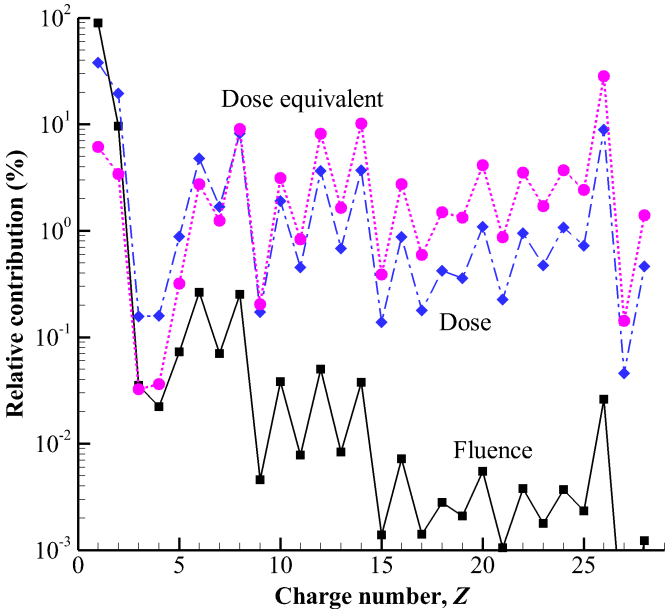

Figure 1.1: Fluence, dose, dose equivalent of different elements of the free-space GCR environment during solar minimum expressed in relative contribution [7].

and electrons and positrons (2%); these leptons, however, are not considered a risk for human missions due to their too low intensities.
As shown in Fig. 1.1, the baryonic component is mainly composed of hydrogen ions (87%), followed by helium ions (12%), while all other ions are present in a much lower percentage (around 1%). These heavier ions, which possess an atomic number greater than or equal to 3 ($Z \geq 3$), are frequently referred to as *high nuclear charge Z and energy E* (HZE) particles. Despite their low abundance in the spectrum, they have a major impact on health risks. Indeed, the dose and effective dose contribution from HZE particles is non-negligible, accounting for approximately 8% in the reference scenario considered by [7].
Galactic cosmic ray particles exhibit a broad energy spectrum, ranging from a few keV/u up to a maximum peak around 1 GeV/u for all ions.

The GCR flux is modulated by solar activity, which follows an approximate 11-year cycle driven by periodic fluctuations in the Sun magnetic field. Approximately every 11 years, the Sun's magnetic poles reverse; this period of reversal corresponds to a Solar Maximum, whereas a Solar Minimum is associated with periods of relative magnetic stability and lower solar activity. Higher solar activity implies enhanced solar magnetic shielding throughout the heliosphere compared to periods of minimum activity. Consequently, the GCR intensity is inversely correlated with the solar cycle, reaching its minimum during a Solar Maximum

and its peak during a Solar Minimum.

1.1.2 Solar particle events (SPEs)

In contrast to Galactic Cosmic Rays, which represent a steady, continuous background of deep-space radiation, solar radiation consists of particles emitted directly by the Sun, characterized by highly dynamic and episodic behaviors [2]. This solar component can be divided into a continuous emission (the solar wind) and transient, highly intense outbursts known as Solar Particle Events (SPEs). The solar wind is a continuous, low-energy flow of particles, composed mainly of protons and electrons. Their kinetic energy is sufficiently low that these particles are entirely stopped within the first few hundreds of nanometers of human skin; consequently, the solar wind itself is not considered a direct hazard in radiation protection. Nonetheless, its indirect role is significant: during periods of high solar activity, the enhanced emission of the solar wind, together with the altered heliospheric magnetic field, strengthens the magnetic barrier against incoming GCRs, thereby reducing the overall GCR fluence within the solar system [6].

The other type of radiation emitted by the Sun consists of sudden local outbursts of particles with large amounts of energy [5]. These particles are mainly protons, but also include helium and highly charged ions [8]. This phenomenon is known as solar particle events (SPEs), and the particles can be accelerated by solar flares close to the Sun or by coronal mass ejection (CME) shocks in interplanetary space.
The frequency and magnitude of SPEs can vary significantly: when the Sun is in its most active phase, the occurrence of SPEs can reach several events per day, dropping to less than one per week during the least active phase. Moreover, SPEs can vary in size. Large events are characterized by an extremely high total fluence; in these cases, the fluence of protons with energies greater than 30 MeV can exceed 10^9 cm^{-2} over several hours or days [8]. The critical issue is that, although these large SPEs occur rarely (only one or two per 11-year solar cycle over the last sixty years), exposure to such a massive amount of radiation could be lethal for the crew if not properly shielded. The maximum energy of these protons is generally less than 250 MeV/n, with the differential fluence decreasing continuously as energy increases [6]. With a relatively thin layer of shielding, the majority of SPE particles can be stopped; consequently, the primary risks concern tissues near the body surface or activities performed during EVAs (Extra-Vehicular Activities), where shielding is significantly poorer [6]. Therefore, the standard approach in

space radiation protection is to model and evaluate worst-case reference scenarios based on historical observations. For example, some of the most severe events took place in 1956, 1960, 1972, and during August, September, and October of 1989; the proton integral fluence spectra for these specific events are shown in Figure 1.2 [6]

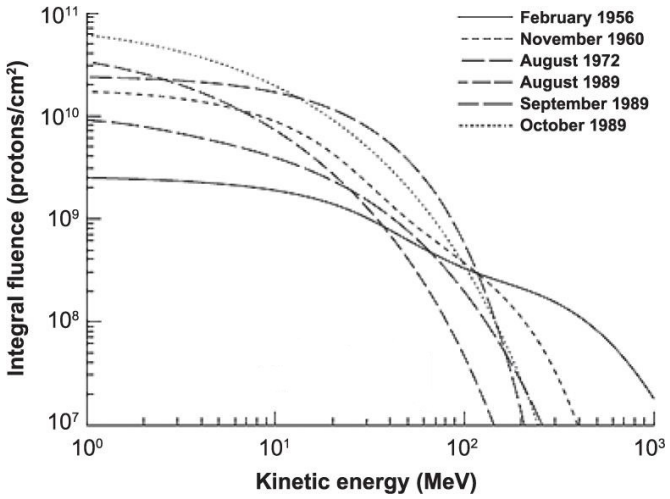

Figure 1.2: Proton integral fluence of intense SPEs.

As shown in the figure, the proton integral fluence is a continuous function of kinetic energy. Certain events, such as the February 1956 SPE, exhibit a harder spectrum, maintaining a significant population of protons at higher energies. Conversely, other events, such as that of August 1972, display a softer spectrum but feature a much higher intensity of lower-energy protons.
Because of this large amount of low-energy protons, the August 1972 event is usually studied as the reference worst-case scenario and, for this reason, it will be the event studied in this work [4].

1.1.3 The August 1972 event

The SPE of August 1972 occurred between the NASA Apollo 16 and Apollo 17 lunar missions during solar cycle 20 [9]. The most significant detected solar flare activity occurred from August 2 to August 11; on August 4, the largest flare recorded in human history took place, which triggered an extreme solar particle event and an intense geomagnetic storm on Earth.
A visible effect of the storm was a widespread series of electric and communication grid disturbances through large portions of North America, as well as satellite disruptions. However, a more curious consequence was the accidental detonation of numerous U.S. naval mines near Haiphong, North Vietnam. These mines were

Destructor (DST) sea mines, which were magnetically sensitive and designed to detonate when magnetic variations exceeded preset thresholds for one or more magnetic factors (e.g., amplitude, polarity, rate of change, and/or gradient).
Until that event, it was well known that solar storms caused terrestrial geomagnetic disturbances, but it was as yet unknown to the military whether these effects could be sufficiently intense to trigger ordnance. As a consequence of the August 1972 event, the U.S. Navy replaced its magnetic-influence-only mines with magneto-seismic mines [9], [10], [11] .

1.2 Dosimetric quantities

This section is dedicated to describing the fundamental definitions of the quantities used to describe the biological effects of radiation on living matter.
The first concept to introduce is Linear Energy Transfer (LET). As charged particles traverse a medium, they lose energy primarily via ionization, producing secondary electrons. The restricted LET, LET_Δ, is defined as the mean energy dE imparted locally to the target material by the incident particle per unit path length dx, excluding energy transfers that produce secondary electrons above a given energy threshold Δ:

$$LET_\Delta = \left(\frac{dE}{dx}\right)_\Delta \tag{1.1}$$

and it is usually expressed in keV/μm. When all energy transfers are considered, and assuming a low-energy secondary electron transport where the range of secondary electrons is negligible, the unrestricted LET, LET_∞, approaches the collision stopping power. This quantity is defined as the average value of energy lost by the incident particle per unit path length due to collisions.
Depending on how energy is deposited along the track structure, and thus depending on the LET, the type of damage produced varies. More densely ionizing particles create a higher concentration of ionized molecules along their path, thereby inducing greater biological damage, whereas sparsely ionizing particles create a less dense concentration of damage, which is thus easier for the cell to repair.
A fundamental physical quantity used in radiobiology is the *absorbed dose*, defined as the average energy dE deposited by radiation per unit mass dm of a medium:

$$D = \frac{dE}{dm} \tag{1.2}$$

and its unit of measurement is the gray (Gy), which is equivalent to 1 joule of radiation energy absorbed per kilogram of matter (1 Gy = 1 J/kg). For a monoenergetic charged-particle field under simplified conditions, the absorbed dose can be related to the LET through the particle fluence, $\Phi = N/A$ (where N is the number of particles traversing a unit surface A perpendicular to the direction of propagation):

$$D = \frac{N}{A}\frac{dE/dx}{\rho} = \Phi\frac{1}{\rho}\frac{dE}{dx} \tag{1.3}$$

Even if there is a strong correlation between absorbed dose and biological response, other quantities such as *equivalent dose* and *effective dose* must be introduced to better correlate radiation exposure with biological effects. These are radiation protection quantities rather than purely physical quantities; they can vary over time, are not universal, and are defined specifically for radiation protection purposes.

The primary consideration is that the same energy deposited into the same mass of matter can produce different biological effects depending on the type of radiation. This is of particular importance in the space environment, where the radiation spectrum consists of various types of particles.

For this purpose, the International Commision on Radiological Protection (ICRP) defined the *equivalent dose*, H_T, in an organ or tissue T irradiated by radiation type R as:

$$H_T = \sum_R w_R D_{R,T} \tag{1.4}$$

The unit of measurement for equivalent dose is the Sievert (Sv); for photons, which are taken as the reference radiation, 1 Sv = 1 Gy = 1 J/kg. The term w_R is called the *radiation weighting factor*; it is dimensionless and reflects the relative effectiveness of different radiation types for radiation protection purposes. The values of the radiation weighting factor change depending solely on the particle type and, with the exception of neutrons, are independent of the particle's energy. These w_R values are listed in Table 1.1 according to the ICRP guidelines, where photons are used as the reference radiation with a weighting factor $w_R = 1$.

The equivalent dose greatly simplifies the evaluation of the effects of different particles in an organ or tissue; however, it provides sufficient precision for radiation protection applications, particularly in low-dose and low-dose-rate situations and where stochastic effects are dominant. In space radiation environments,

Radiation type	w_R
Photons	1
Electrons and muons	1
Protons and charged pions	2
Alpha particles and heavy ions	20
Neutrons	2-20

Table 1.1: Radiation weighting factors according to the ICRP [12]

however, dose rates can be high, and numerous highly energetic ions are present. Consequently, using a constant value of $w_R = 20$ for all heavy ions is overly simplified.

A better approach for space dosimetry, defined by the ICRU (International Commission on Radiation Units and Measurements), is to use the *dose equivalent*. This quantity distinguishes the biological effectiveness of different radiations by introducing quality factors, Q(LET), which account for the variation of biological effects with LET in water. The dose equivalent at a point is defined as:

$$H_{T,Q} = Q_T D_T \tag{1.5}$$

where D_T is the mean absorbed dose in the organ or tissue T for the given radiation field R:

$$D_T = \sum_R = D_{T,R} \tag{1.6}$$

and Q_T is the mean quality factor

$$Q_T = \frac{1}{m_T D_T} \int_{m_T} \int_{L=0}^{L=\infty} Q(L) D_L dL dm \tag{1.7}$$

where m_T is the mass of the organ or tissue T, $D_L = \frac{dD}{dL}$ is the distribution of the absorbed dose as a function of LET at the point of interest within the tissue, and $Q(L)$ is the quality factor as a function of LET in water, defined in [12] as:

$$Q(L) = \begin{cases} 1, & \text{for } LET < 10 keV/\mu m \\ 0.32 LET - 2.2, & \text{for } 10 < LET < 100 keV/\mu m \\ 300\sqrt{LET}, & \text{for } LET > 100 keV/\mu m \end{cases} \tag{1.8}$$

Other essential radiation protection quantities are the *effective dose*, E, and the *effective dose equivalent*, H_E, which account for the fact that the same equivalent dose deposited in different organs can lead to different risks due to varying

radiosensitivities. The *effective dose equivalent*, H_E, is frequently employed in space radiation protection analyses. The effective dose is defined as:

$$E = \sum_T w_T H_T \tag{1.9}$$

where w_T is the tissue weighting factor defined in Table 1.2, and H_T is the equivalent dose averaged over the male and female organs or tissues T ($H_T = 0.5(H_T^M + H_T^F)$). Like the equivalent dose, the effective dose is measured in Sieverts (Sv).

The *effective dose equivalent* is the quantity corresponding to the dose equivalent, $H_{T,Q}$, used in place of the effective dose when evaluating radiation quality through LET-dependent quality factors, $Q(L)$, instead of fixed radiation weighting factors, w_R. The effective dose equivalent, H_E, is defined as:

$$H_E = \sum_T w_T H_{T,Q} \tag{1.10}$$

where w_T represents the tissue weighting factors listed in Table 1.2, and $H_{T,Q}$ is the mean dose equivalent averaged over male and female organs or tissues T ($H_{T,Q} = 0.5(H_{T,Q}^M + H_{T,Q}^F)$). Furthermore, gender-specific effective dose equivalents (H_E^M and H_E^F) are defined as follows :

$$H_E^M = \sum_T w_T H_{T,Q}^M \tag{1.11}$$

$$H_E^F = \sum_T w_T H_{T,Q}^F \tag{1.12}$$

Organ or tissue	w_T	$\sum w_T$
Red bone marrow, colon, lung, stomach, breast, remainder tissues*	0.12	0.72
Gonads	0.08	0.08
Bladder, esophagus, liver, thyroid	0.04	0.16
Endosteum (bone surface), brain, salivary glands, skin	0.01	0.04
Total		1.00

Table 1.2: Tissue weighting factors in according with ICRP 103(2007)
*remainder tissues: adrenals, extrathoracic region, gall bladder, heart, kidneys, lymphatic nodes, muscle, oral mucosa, pancreas, prostate (male) small intestine, spleen, thymus, and uterus/cervix (female)

The tissue weighting factor, w_T, is a dimensionless factor by which the equivalent dose and the dose equivalent are weighted to represent the relative contribution

of that tissue to the total health detriment resulting from uniform irradiation. Note that, by definition:

$$\sum_T w_T = 1 \tag{1.13}$$

The last key concept to introduce is the Relative Biological Effectiveness (RBE) which serves as a quantitative indicator of the effectiveness of a given radiation type compared to a reference radiation in inducing a specific biological endpoint in a particular target under defined exposure conditions. The RBE is formally defined as the ratio between the absorbed dose of a reference radiation (D_{ref}) and the absorbed dose of the radiation of interest (D) required to produce the same biological effect. Mathematically, it is expressed as:

$$RBE = \left.\frac{D_{ref}}{D}\right|_{iso,SF} \tag{1.14}$$

Consequently, a higher RBE indicates that the considered radiation quality is more effective than the reference radiation at achieving the specified biological effect at that dose level [13]. As evident from this definition, the RBE depends not only on a predefined biological endpoint (e.g., cell survival or chromosomal damage) but also on various biological variables (such as cell type, cell cycle phase, and oxygenation) and physical parameters (including dose, dose rate, particle energy, and track structure).
By implementing the RBE, it is possible to introduce the *RBE-weighted mean absorbed dose*, $D_{T,\mathrm{RBE}}$, which is particularly important at high doses where tissue reactions (deterministic effects) may occur. In this high-dose regime, w_R and $Q(L)$ cannot be properly applied because they are defined specifically for the low-dose range. The RBE-weighted mean absorbed dose assesses non-stochastic risks at high doses and is of particular importance in the space environment; for instance, as will be described in Section 1.4.1, NASA uses this quantity to establish limits for deterministic risks. The RBE-weighted mean absorbed dose is defined as:

$$D_{T,\mathrm{RBE}} = \mathrm{RBE} \cdot D_T \tag{1.15}$$

and is measured in Gray equivalents (Gy-Eq). Because the RBE depends on the specific particle type producing the damage, the dose, the dose rate, and the organ or tissue involved, $D_{T,\mathrm{RBE}}$ effectively accounts for all of these factors.

The quantities described in this section are fundamental for radioprotection and are used to evaluate the exposure risk for astronauts and to set the limits.

1.3 Radiation risks for astronauts

In the space environment, space radiation can cause various biological effects, which can be categorized either as acute health risks (which immediately compromise mission success) or late effects (experienced years after exposure). Acute effects occur when a large dose of radiation is received over a short amount of time, as in the case during SPE, while late effects are more closely associated with chronic exposure.
Alternatively, biological effects can be classified into tissue reactions and stochastic effects.
Tissue reactions (also termed deterministic effects) appear only after a specific threshold dose is exceeded. The severity of the effect increases with dose, and the damage is manifest in all exposed individuals who receive a dose higher than the threshold. They usually occur early (days or weeks after the exposure), but in some cases can also occur later (for example cataract can appear 20 years after radiation exposure).
In contrast, stochastic effects are assumed to have no threshold; their probability of occurrence increases with the dose, whereas their severity is independent of it. These effects are typically diagnosed several years after exposure.
Regarding the risk categories faced by astronauts on long-duration missions, NASA's Space Radiation Element (SRE) has identified four distinct categories: carcinogenesis, acute and late Central Nervous System (CNS) effects, degenerative tissue effects, and Acute Radiation Syndrome (ARS).

Regarding carcinogenesis, this is a late effect that can be caused by both chronic exposure to low dose-rate GCRs and acute exposure to SPEs. The primary contribution to this risk comes from GCRs, while SPEs act to further compound it. Carcinogenesis is classified as a late effect because it can originate from changes in a small number of cells. Furthermore, carcinogenesis is classified as a stochastic effect to highlight the predominant role of chance in its occurrence, arising from the random nature of radiation interactions, which leads to significant statistical fluctuations. A certain level of risk is present even at very low doses [14].
Evidence of radiation-induced cancer risk is derived primarily from epidemiological data on low-LET radiation exposure including atomic bomb survivors, radiation workers, and radiotherapy patients. These data are subsequently scaled

to account for the different radiation types and dose rates encountered in space. Finally, current cancer risk estimates provide strong evidence for both sex- and age-dependent variations.

Regarding the CNS, both acute and late effects can be induced by space radiation. Acute CNS risks consist of alterations in cognitive and motor functions, whereas late effects include neurological disorders such as premature aging, Alzheimer's disease, and dementia.

The third category of risk identified by NASA's SRE encompasses degenerative tissue effects, which include cardiovascular, cataracts, digestive, and respiratory diseases. These effects have been studied extensively following exposure to terrestrial low-LET radiation, allowing researchers to postulate similar outcomes after space radiation exposure. However, the differences between the space radiation environment and that of Earth introduce significant uncertainties into these risk estimations [14].

The final category is ARS, which comprises highly severe syndromes that manifest at high doses. For this reason, ARS could be experienced in the space environment during an intense SPE in a poorly shielded scenario, such as during an EVA.
ARS symptoms appear shortly after irradiation. First, a prodromal phase occurs, followed by a latent period (which can last from hours to weeks). Subsequently, three distinct syndromes may manifest: the hematopoietic syndrome, the gastrointestinal syndrome, or the cerebrovascular syndrome. The hematopoietic syndrome occurs at radiation doses of 2.5–5 Gy due to the insufficient production of red blood cells, white blood cells, and platelets; if death occurs, it typically happens approximately 60 days after exposure.
The gastrointestinal syndrome appears at higher doses, around 5–12 Gy, with death potentially occurring within 3–10 days; its primary cause is the depopulation of the epithelial lining of the gastrointestinal tract. The cerebrovascular syndrome manifests at extremely high doses, typically exceeding 50 Gy, leading to death within 1–2 days. The exact cause of death is not fully understood, largely because there are very few documented cases of human beings exposed to such high doses.

1.4 Radiation protection in space missions

In space missions, the crew is exposed to large quantities of radiation due to GCRs and SPEs, and exposure limits are set by the various space agencies. Before applying these limits, according to radiation protection principles, both the Justification and Optimization of radiation exposure are necessary. Justification means that the individual or societal benefit resulting from the practice outweighs the health detriment that it may cause. Optimization means reducing the magnitude of individual doses, the likelihood of exposure, and the number of individuals exposed, adhering to the *As Low As Reasonably Achievable* (ALARA) principle while taking into account the current state of technical knowledge as well as economic and societal factors. Justification, optimization, and dose limits are protection principles valid in general (not only in the space field) but are also applied to patients and other occupationally exposed workers.

1.4.1 Exposure limits and operational constraints

Concerning exposure limits for astronauts, these criteria vary depending on the specific space agency; thus, the National Aeronautics and Space Administration (NASA), the European Space Agency (ESA), the Russian Space Agency (RSA), the Canadian Space Agency (CSA) and the Japan Aerospace Exploration Agency (JAXA) can have different exposure limits.
The limits set by agency are divided depending on deterministic or stochastic effects.
Regarding the former, limits are set to specific organs: skin, eye and BFO (blood forming organs -primary active bone marrow, spleen, and lymph nodes); at this list NASA adds heart and CNS and JAXA testes. The limits are reported in tables 1.3 1.4, 1.5; note that NASA's limits are expressed in Gy-Eq while the other agencies express them in Sv. RSA in addition to the limits in Tab. 1.4 established career limits for eye (2.0 Sv), skin (6.0 Sv) and an acute limit of 0.15 Sv for BFO.

Concerning stochastic effects, exposure limits are expressed in terms of effective dose. For ESA, RSA, and CSA, the career limit is set to 1 Sv, independent of the astronaut's age and sex, whereas for NASA, the limit is 600 mSv. This NASA value was obtained by applying the risk model to the most susceptible case, which corresponds to a 30-year-old female. JAXA, however, implements sex- and age-dependent limits based on a 3% Lifetime Cancer Mortality (LCM)

	30-Day Limit	1-Year Limit	Career Limit
Skin	1.5	3.0	6.0
Eye	1.0	2.0	4.0
BFO	0.25	0.5	Not Applicable
Heart	0.25	0.5	1.0
CNS	0.5	1.0	1.5
CNS (Z>9)	Not Applicable	0.10	0.25

Table 1.3: NASA limits for deterministic effects (in Gy-Eq) [15]

	30-Day Limit	1-Year Limit
Skin	1.5	3.0
Eye	0.5	1.0
BFO	0.25	0.5

Table 1.4: ESA and RSA limits for deterministic effects (in Sv) [16]

	30-Day Limit	1-Year Limit	Career Limit
Skin	2.0	7.0	20.0
Eye	0.5	2.0	5.0
BFO	Not Applicable	0.5	Not Applicable
testes	Not Applicable	1.0	Not Applicable

Table 1.5: JAXA limits for deterministic effects (in Sv) [16]

threshold, as reported in Table 1.6. Until 2020, NASA also used sex- and age-dependent limits; however, these were based on a 3% Risk of Exposure-Induced Death (REID) calculated within a 95% confidence interval.

Age at First Space Flight	Male	Female
27-30	0.60	0.50
31-35	0.70	0.60
36-40	0.80	0.65
41-45	0.95	0.75
>45	1.00	0.80

Table 1.6: Career limits imposed by JAXA expressed in Effective dose (Sv) [17]

Regarding operational constraints to minimize radiation exposure, the standard practices in radiation protection are increasing the distance from the source and reducing the exposure time. However, these methods, while easily applied to patients and occupationally exposed workers, are not applicable in the space field because cosmic radiation is isotropic (making it impossible to increase the distance from the source) and the exposure time is dictated by the duration required for the mission. Therefore, shielding remains the primary physical mitigation strat-

egy available in space, although complete protection through shielding cannot be entirely achieved.

1.5 Biological effects in space missions

As previously mentioned in Section 1.3, radiation poses a significant health risk to human beings, and this risk is even higher in the space environment due to GCRs and SPEs. This section provides a brief overview of the biological mechanisms underlying these risks.

Ionizing radiation is harmful to biological tissues because it possesses sufficient energy to detach electrons from atoms or molecules. The radiation can damage biological structures either directly, by breaking the chemical bonds of critical biomolecules, or indirectly, by interacting with other cellular molecules (predominantly water) to produce free radicals that diffuse and induce oxidative damage.
Radiation interacts with cells in their entirety, affecting the cytoplasm, mitochondria, and Golgi apparatus; however, the critical target for biological effects is widely identified as the DNA molecule. Inside the cell nucleus, DNA is tightly coiled around histone proteins to form threadlike, rod-shaped structures known as chromosomes, which condense visibly just before cell division. Consequently, when radiation interacts with this structured genetic material, different types of DNA damage can occur.
Radiation can induce various types of DNA lesions. The simplest form is base damage, which consists of alterations to the chemical structure of a nitrogenous base or the breakage of hydrogen bonds. Another type of damage involves disruptions in the sugar-phosphate backbone of only one strand of the double helix, known as Single-Strand Breaks (SSBs). These can lead to genetic alterations only if they remain unrepaired or are repaired incorrectly; however, because SSBs can be efficiently repaired by cellular mechanisms, they generally have low biological significance.
Conversely, when two SSBs occur on opposite strands and are separated by fewer than approximately 10 base pairs, a more severe lesion known as a Double-Strand Break (DSB) is formed. DSBs are significantly more difficult to repair than SSBs and, for this reason, pose a much greater challenge to cell survival. Regarding ionizing particles, those with high LET (such as HZE ions found in GCRs and SPEs) can produce a higher yield of clustered DNA lesions. These complex types

of damage are highly refractory to repair, leading to more severe biological outcomes, including cell death, carcinogenesis, and mutagenesis.
Ultimately, these DSBs can manifest as structural changes in the chromosomes themselves. When a chromosome suffers multiple breaks, it splits into fragments. These fragments may rejoin correctly, fail to rejoin at all, or misrejoin with fragments from different chromosomes. The latter two scenarios give rise to structural modifications known as aberrations, which are typically scored during the subsequent mitosis.
If cells are irradiated prior to DNA synthesis (early in interphase), the resulting damages are termed *chromosome aberrations*. In this case, a single strand of chromatin is broken, and the break is replicated during the synthesis (S) phase of the cell cycle. Alternatively, *chromatid aberrations* occur when the cell is irradiated later in interphase (after DNA synthesis); here, the breaks can occur independently in one or both sister chromatids. These aberrations can either be lethal, leading to cell death, or compatible with cell viability, potentially resulting in carcinogenesis.
The two primary types of lethal chromosome aberrations are dicentrics and centric rings. Dicentric aberration occurs when two different broken chromosomes incorrectly join together; this process creates an abnormal chromosome with two centromeres, along with a separate acentric fragment (a piece without a centromere). Centric rings, instead, happen when two breaks occur in the same chromosome (one in each arm). The sticky ends of the central segment rejoin with each other to form a ring containing the centromere, while the outer ends fuse into an acentric fragment.
A classic lethal chromatid aberration is the anaphase bridge. In contrast, the two main types of non-lethal chromatid aberrations are translocations and deletions. A translocation involves an exchange of genetic material between two chromosomes where the overall structure appears superficially unchanged, whereas a deletion involves the definitive loss of a chromosomal fragment.

As previously mentioned, the cell type influences the biological response, which led in Section 1.2 to the introduction of RBE-weighted absorbed dose that is then evaluated in acute or protracted irradiation condition. Similarly, the exposure limits imposed by space agencies and described in Section 1.4.1 depend heavily on the specific tissues involved. For this reason, it is fundamental to develop a radiobiological model that is sensitive to the type of tissue irradiated, and that consequently adapts its predictions depending on the specific cell line.

In other words, a cell specific radiobiological model is necessary.
In past space radiation studies, to evaluate tissue reactions, the BIANCA biophysical model (described in Chapter 2.1.3) was used to study cell death exclusively in fibroblasts. Therefore, this work aims to extend the model to other cell lines, enabling more realistic predictions of dosimetric quantities for direct comparison with radiation protection limits. In particular, the chosen cell lines can be representative of breast and skin tissues, on which this work focuses.

CHAPTER 2

Material and methods

This chapter presents the computational framework and theoretical methods used to evaluate the biological effects of space radiation on astronauts. A major objective of this work is the generation of cell-specific radiobiological databases for normal human skin and breast tissues consisting of radiobiological parameters for various ions as a function of Linear Energy Transfer (LET). The following sections describe the methodology adopted to achieve this objective, together with the computational framework used to apply these databases to space radiation studies.

First, the radiobiological models employed to predict cell survival are presented, with particular emphasis on the BIANCA model. Next, the methodology used to develop the radiobiological databases is described, including the characterization of the selected cell lines and the derivation of the parameters governing their respective survival curves. Finally, the particle transport simulations through the human body are addressed, focusing on the FLUKA Monte Carlo code and its application to space radiation studies.

2.1 Radiobiological Modeling

This section provides an introduction to the radiobiological models used in this work. First, the Linear-Quadratic model, the most widely used mathematical framework for describing the relationship between cell survival and the delivered dose, is presented. Next, the Lea-Catcheside factor, which extends the LQ model

to account for dose-rate effects, is introduced. Finally, the BIANCA model, used to predict cell death and chromosome aberrations in specific cell lines irradiated with ions, is described.

2.1.1 Linear-Quadratic model

The Linear-Quadratic (LQ) model is the standard framework for representing the relationship between cell survival and delivered radiation dose. It is widely used to characterize radiation effects in both laboratory and clinical settings, remaining the standard model in radiobiology.
Historically, the LQ model was not the first biological model developed. The earliest approach was the *single-target model*, established at the beginning of the 20th century. In this model, a cell survives only if it experiences no hits; thus, the relationship between cell survival and dose is purely exponential, as described by Equation 2.1:

$$S = e^{-D/D_0} \tag{2.1}$$

where D is the delivered dose and D_0 represents the dose that leads to an average of one hit per cell. According to this model, a 1:1 correlation exists between $\ln(S)$ and the average number of lethal lesion per cell.

Around the second half of the 20th century, the *single-hit, multi-target model* became the most common approach. Within this framework, a cell is conceptualized as being composed of m distinct targets, each of which must be inactivated for cell death to occur. Unlike the previous model, which assumed a single radiosensitive target, a single hit is sufficient to "inactivate" an individual target, but hitting multiple targets is required to fully inactivate the cell.
For instance, the geneticist Theodor Puck and the virologist Philip I. Marcus utilized a value of $m = 2$, justifying it by the diploid nature of human cells. However, subsequent studies revealed that the parameter m can assume a broad range of values and is often interpreted merely as an empirical descriptive factor. According to the single-hit, multi-target model, the survival probability is described by Equation 2.2:

$$S = 1 - (1 - e^{-D/D_0})^m \tag{2.2}$$

where the ratio D/D_0 represents the average number of hits per target.

The most modern model, which has replaced its two predecessors, is the *Linear-Quadratic model*, postulated by several authors based on different biophysical justifications. For example, some authors describe it as a combination of damage resulting from single-track and multi-track events, while others employ a mechanistic approach based on the yield of DNA Double-Strand Breaks (DSBs).
The standard expression of the LQ model is given by Equation 2.3:

$$S = e^{-(\alpha D + \beta D^2)} \tag{2.3}$$

where D is the absorbed dose delivered to the cells, while α and β are parameters characteristic of the specific cell line. These coefficients quantify the cell's radiosensitivity; since the SI unit for absorbed dose is the gray (Gy), α is expressed in Gy^{-1} and β in Gy^{-2}.
The cell survival probability is typically plotted on a logarithmic scale as a function of dose. The α and β parameters are referred to as the *linear* and *quadratic* terms, respectively. Under a widely accepted biophysical interpretation, α reflects cell death due to a single-hit event (i.e., lethal damage caused by a single incident particle track), whereas β represents cell death resulting from multiple hits (the interaction of sub-lethal lesions produced by different radiation tracks), which scales proportionally to the square of the dose.
A frequently utilized parameter is the α/β ratio, which represents the dose at which the linear and quadratic contributions to cell killing are precisely equal:

$$\alpha D = \beta D^2 \Rightarrow D = \alpha/\beta \tag{2.4}$$

A high α/β ratio indicates that the linear term dominates, meaning that the survival curve exhibits a predominantly linear behavior on a semi-logarithmic plot. Conversely, a low α/β ratio results in a more pronounced downward curvature. These two behaviors are illustrated in Figure 2.1 [18].

Densely ionizing particles (high-LET radiation) are more likely to exhibit a purely linear survival behavior with a dominant α component, because a single particle track is often sufficient to induce complex, lethal chromosomal aberrations. In contrast, sparsely ionizing radiation (such as X-rays or gamma rays) tends to show a more pronounced curvature; this occurs because there is a higher probability that lethal aberrations result from the spatial and temporal interaction of sub-lethal damage caused by two independent radiation tracks.
The parameters governing the survival curve vary significantly depending on the cell line, the specific phase of the cell cycle, and environmental factors such as

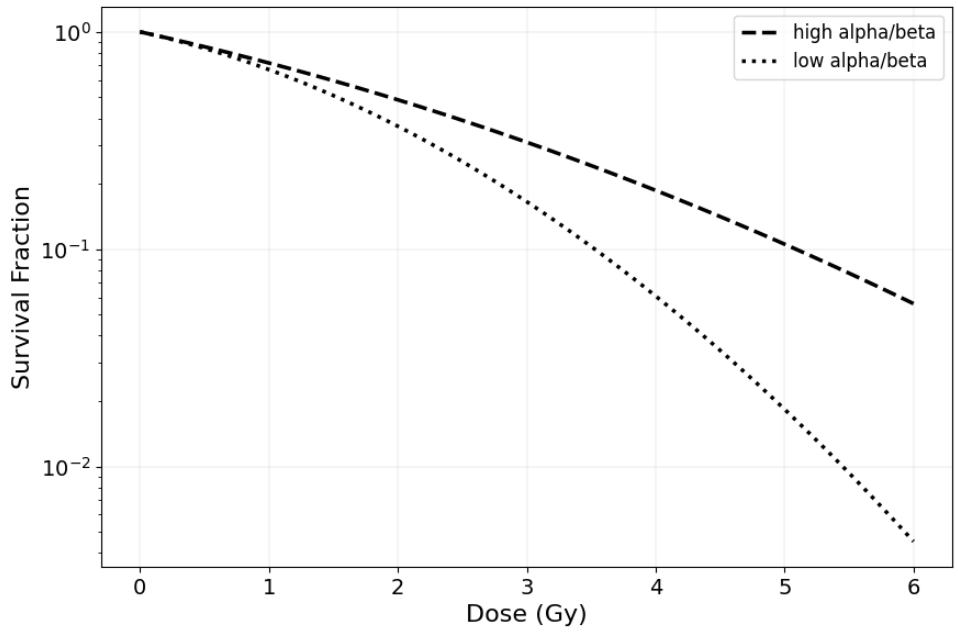

Figure 2.1: LQ model curves with high (10 Gy) and low (3 Gy) α/β ratio are shown as dashed and dotted lines, respectively.

oxygen concentration. However, a comprehensive description of these biological modifiers remains beyond the scope of this work.

2.1.2 Sublethal damage repair

The conventional linear-quadratic expression for survival probability (Eq. 2.3) is typically used to describe acute irradiation. However, the formula must be modified for fractionated or low-dose-rate exposures. In the context of this work, considering low-dose-rate exposure is crucial, as SPEs can last from a few hours to several days.

The *Lea-Catcheside factor* (also known as the *dose protraction factor*), denoted as $G(t)$, quantifies the reduction in the probability of sub-lethal lesion interactions due to cellular repair mechanisms operating over time. In other words, it accounts for the cell's capacity to repair sub-lethal damage during the irradiation period before a secondary damaging event occurs. Consequently, this factor modifies the quadratic term (β), transforming Equation 2.3 into Equation 2.5 [19]:

$$S = e^{-(\alpha D + G(t)\beta D^2)} \tag{2.5}$$

The value of $G(t)$ strictly ranges between zero and one [20]. At high dose rates,

$G(t)$ approaches unity, and Equation 2.5 reduces to the conventional LQ model (Eq. 2.3). Conversely, as the dose rate decreases, $G(t)$ diminishes; this leads to an increase in the survival fraction, reflecting the progressive repair of sub-lethal damage during the exposure [19].
Two distinct mathematical formalisms exist for $G(t)$: one tailored to fractionated regimens and another for continuous low-dose-rate irradiation. While this work focuses primarily on the latter due to the protracted nature of SPEs, the formulation for fractionated exposures is also presented here for completeness.

In the case of fractionated radiation, the biological effects of multiple discrete exposure events must be aggregated. The factor G is expressed as follows (Eq. 2.6):

$$G = \frac{1}{n}\left[1 + \frac{2}{n}\frac{e^{-\mu T_i}}{1 - e^{-\mu T_i}}\left(n - \frac{1 - (e^{-\mu T_i})^n}{1 - e^{-\mu T_i}}\right)\right] \tag{2.6}$$

where n is the number of irradiation fractions, T_i denotes the time interval between subsequent fractions, and μ represents the repair rate constant.

Conversely, for continuous low-dose-rate irradiation, the repair dynamics occurs progressively during the exposure, necessitating a continuous-time integration. In this scenario, $G(t)$ is given by Equation 2.7:

$$G = \frac{2}{\mu T}\left(1 - \frac{1 - e^{-\mu T}}{\mu T}\right) \tag{2.7}$$

where T is the total irradiation duration and μ represents the repair rate constant [19], which is related to the repair half-time $T_{1/2}$ via the relation $\mu = \ln(2)/T_{1/2}$. The kinetics of sub-lethal damage repair are frequently described using a biphasic repair model, which incorporates both a fast and a slow component [21]. These two components can be better understood by examining the underlying DNA repair pathways. DNA damage can be processed through a fast pathway, which operates on a timescale of minutes to an hour and primarily involves mechanisms such as Non-Homologous End Joining (NHEJ). Alternatively, repair can proceed via a slower pathway extending over several hours, utilizing Homologous Recombination (HR) or other multi-step enzymatic processes [19].
Consequently, it becomes necessary to evaluate both the fast and slow components of the repair kinetics (G_{fast} and G_{slow}), as well as their respective contributions to the overall recovery process. The total Lea-Catcheside factor G can be thus

expressed as a linear combination (Eq. 2.8):

$$G = a_{\mathrm{f}} G_{\mathrm{fast}} + a_{\mathrm{s}} G_{\mathrm{slow}} \tag{2.8}$$

where a_{f} and a_{s} represent the fractions of the fast and slow repair components, respectively, satisfying the condition $a_{\mathrm{f}} + a_{\mathrm{s}} = 1$.

2.1.3 The BIANCA model

In this work, BIANCA was used to predict dose-response curves for clonogenic cell survival in different cell lines irradiated with ions at various LET values. Through the BIANCA input parameters, the user can select the radiation type responsible for the damage together with the corresponding energy and LET values. To construct the radiobiological databases used in this work, the available experimental data were grouped into five ion categories: (1) protons ($Z = 1$); (2) Helium and Lithium ($Z = 2$–3); (3) Beryllium, Boron, Carbon, Nitrogen and Oxygen ($4 \leq Z \leq 8$); (4) ions with atomic number between Fluorine and Silicon ($9 \leq Z \leq 14$); and (5) elements heavier than Silicon ($Z \geq 15$) [22–24]. This grouping was adopted because experimental radiobiological data are not available for every ion species. Since the model is parameterized as a function of LET, ions with similar atomic numbers were assumed to exhibit comparable radiobiological behavior for a given LET range, allowing a common parameterization to be derived for each group.

BIANCA relies on the three following assumptions:

- Ionizing radiation can induce DNA *Critical Lesions* (CLs) where a CL is defined as a damage to the double helix that is severe enough to produce two (main) independent chromosome fragments;
- Chromosomal aberrations can form due to incorrect rejoining of these fragments, or their failure rejoin. Both processes depend on the distance between fragments;
- Lethal aberrations, such as dicentrics, rings and large deletions (where 'large' means visible when chromatin is condensed) lead to cell death.

The main concept that underlies BIANCA is that some of the various DNA damage types induced by ionizing radiation are 'critical' for the cell fate, because they give rise to chromosomal fragments that, in turn, following incorrect rejoining or unrejoining, can lead to cell death.

In addition to the radiation parameters (particle type, energy, and LET), BIANCA includes two adjustable parameters related to cell fate: the CL yield (mean number of CLs per unit dose and unit DNA mass) and f, the probability that a fragment remains unrejoined.

Operationally, exposure to ionizing radiation induces a specific CL yield, thereby producing a corresponding number of fragments per unit dose and unit DNA mass. The resulting fragments either remain unrejoined, or rejoin with a probability P that depends on the initial inter-fragment distance r. Based on previous works, the relationship between P and r is modeled as a step function of the initial distance, taking a value of 1 below a threshold distance d and 0 elsewhere. The parameter d is non-adjustable and is kept constant at 0.8 μm in the simulations; this threshold corresponds to the mean distance between two adjacent chromosome territories.
Fragments separated by a distance smaller than d have a specific probability of remaining unrejoined, which is quantified by f. As previously mentioned, f constitutes the second adjustable parameter of the model.

Regarding chromosomal aberrations, the relationship between P and r is described by the exponential function given in Equation 2.9; this relationship was derived from experimental data on specific aberration categories in human lymphocytes:

$$P(r) = e^{-\frac{r}{r_0}} \tag{2.9}$$

where $r_0 = 0.8\mu m$ [22–24].

2.2 Generation of radiobiological databases

The aim of this section is to describe the methodology used to generate cell-specific radiobiological databases for the skin (AG01522 fibroblasts and HaCaT keratinocytes) and breast (MCF10A epithelial cells). First, the investigated cell lines are presented together with the available experimental datasets. Next, the procedure used to derive the radiobiological parameters required by the BIANCA model is described, using the V79 cell line as the reference dataset. Finally, the methodology adopted to extend these databases to different ion species and LET values is presented.

2.2.1 Cell-specific radiobiological databases

Three normal human cell lines were selected to generate tissue-specific radiobiological databases: AG01522 fibroblasts and HaCaT keratinocytes for the skin, and MCF10A epithelial cells for the breast. The following paragraphs summarize the biological characteristics of these cell lines and justify their selection for the development of the corresponding databases.

AG01522 The AG01522 cell line was selected as a representative model of normal human skin fibroblasts for the generation of the skin-specific radiobiological database. It consists of human diploid fibroblasts derived from a three-day-old male neonate. The culture was initiated in 1976 from an explant of minced foreskin removed ante-mortem one day earlier [25, 26]. AG01522 fibroblasts are widely used in radiobiological studies, and an extensive body of experimental data is available for irradiation with various ion species.

Fibroblasts are the principal cells of connective tissue, where they synthesize extracellular matrix proteins such as collagen, provide structural support, and play a central role in tissue repair [27]. Since the experimental data employed in this work include not only AG01522 but also other normal human fibroblast cell lines, the umbrella term Human Skin Fibroblasts (HSF) is used throughout this thesis to collectively refer to these cell types. As the predominant cells of the dermis, fibroblasts represent a relevant model for evaluating radiation-induced biological effects in normal skin [28].

HaCaT The HaCaT cell line was selected to represent the epidermal compartment of the skin in the generation of the skin-specific radiobiological database. It is an immortalized human keratinocyte cell line derived from adult epidermis that retains the ability to proliferate and differentiate similarly to basal keratinocytes in vivo [29, 30].

Keratinocytes constitute approximately 95% of the epidermal cellular population and are therefore the primary target cells of the outermost skin layer. The remaining cells mainly comprise melanocytes, together with smaller populations of Langerhans and Merkel cells [28, 31, 32]. Their high abundance and physiological relevance make HaCaT cells an appropriate model for evaluating radiation-induced biological effects in the epidermis.

MCF10A The MCF10A cell line was selected as a representative model of normal breast epithelium for the generation of the breast-specific radiobiological

database. It is a non-tumorigenic human mammary epithelial cell line established from the mammary gland of a 36-year-old woman with fibrocystic disease and is widely used to investigate the biology and radiation response of normal breast tissue [33].

Normal breast tissue is considered one of the organs of interest for radiation protection in female astronauts because of its radiosensitivity and its relevance in radiation-induced cancer risk. Consequently, MCF10A cells provide an appropriate model for investigating the biological effects of space radiation on healthy breast tissue and for generating a breast-specific radiobiological database.

2.2.2 Generation of α and β cell-specific parameters

The core objective of this work is to predict the response of a new cell line following ion irradiation, given the response of a reference cell line to both photon and ion irradiation, alongside the response of the new cell line to photon irradiation alone.
The V79 cell line (a fibroblast line derived from the Chinese hamster) is selected as the reference due to its widespread use in radiobiology.
The first step consists of determining the two parameters, CL yield and f, for the V79 reference line. This is achieved by using experimental cell survival curves for photons and ions from the literature and reproducing them with BIANCA by adjusting these parameters. For each ion species, the two parameters were fitted as a function of LET, enabling the simulation of the V79 response, in principle, for any arbitrary LET value.
For the V79 cell line the values of CL yield and f for photon irradiation at various energies are presented in table 2.1, while for ion irradiation, the values of CL yield and f are fitted as a function of LET.

	CL ($Gy^{-1}cell^{-1}$)	f
X 250 kVp	1.4	0.08
Co-60	1.1	0.08
6 MV	1.06	0.08

Table 2.1: CL and f values for V79 cells irradiated with photons at different energies

Regarding ions, Equation 2.10 relates the CL yield to the LET:

$$\mathrm{CL}(\mathrm{LET}) = a \cdot \arctan(b \cdot \mathrm{LET} + c \cdot \mathrm{LET}^2) \cdot \ln(1 + d \cdot \mathrm{LET}) \tag{2.10}$$

where the parameters a, b, c, and d depend on the specific ion and are listed in Table 1.
For the ion's f value, the function relating f to LET is described by Equation 2.11 :

$$f(\mathrm{LET}) = \begin{cases} a + \frac{0.08-a}{2} \cdot \mathrm{LET}, & \text{if LET} < X \\ c, & \text{if LET} > X \end{cases} \tag{2.11}$$

where the values of a, c, and X are reported in Table 2. It should be noted that the determination of CL and f values for the V79 cell line under photon and ion irradiation as a function of LET was established in previous work and is adopted here as the foundation for the scaling procedure.

Once the CL yield and f parameters have been determined, BIANCA simulations can be performed to obtain the cell survival probability as a function of dose. These survival curves, simulated across a selected range of LET values, are then fitted with the linear-quadratic model (Eq. 2.3) to construct a radiobiological database for V79 cell survival. This database comprises pairs of α and β coefficients tabulated as a function of ion species and LET, alongside the two corresponding photon coefficients.

Furthermore, if the photon response of a new cell line is known (meaning its photon-specific parameters $\mathrm{CL_X}$ and f_X have been determined), it is possible to derive the ion-specific CL and f values for that cell line irradiated with a given ion at a specific energy and LET. To achieve this, the following scaling relationships are applied:

$$CL = CL_{V79} \left[\frac{CL_X}{CL_{X,V79}} \right] \tag{2.12}$$

where $\mathrm{CL_{V79}}$ and $\mathrm{CL_{X,V79}}$ are the cluster yields for V79 reference cells irradiated with the same ion species and by photons, respectively; and

$$f = f_{V79} + f_X - f_{X,V79} \tag{2.13}$$

where f_V79 and $f_\mathrm{X,V79}$ represent the f parameters for V79 cells under the corresponding ion and photon irradiations, respectively.
Once the CL and f parameters for the new cell line under ion irradiation have been determined, BIANCA is utilized to calculate the clonogenic survival fraction

as a function of dose. The resulting curves are then fitted using the LQ model (Eq. 2.3) to extract the new α and β parameters, which are subsequently used to assemble the final radiobiological database. This database consists of a comprehensive dataset of α and β parameters across various ion types and LET values. Following this step, the Lea-Catcheside correction can be applied as detailed in Section 2.1.2. The description of the experimental data utilized and the resulting databases for the new cell lines are presented in Chapter 3.

Although this work focuses exclusively on clonogenic cell death, BIANCA is also capable of generating databases to simulate the dose-response curves of dicentric chromosomes in human lymphocytes, which are widely recognized as biomarkers for stochastic effects. Analogously to the procedure followed for clonogenic cell survival, the initial step consists of identifying the optimal CL and f parameters that reproduce the experimental dose-response curves for both photons and various ion beams. Subsequently, the relationships of CL versus LET and f versus LET are established for each ion type, followed by BIANCA simulations to determine the corresponding α and β parameters [22–24].

2.3 Transport simulations

This section describes the particle transport simulations performed in this work. First, the fundamentals of the Monte Carlo simulation method are introduced, followed by an overview of the specific features of the FLUKA code, with particular emphasis on the modeling of the August 1972 SPE and the implementation of anthropomorphic phantoms. Finally, the interface between FLUKA and BIANCA biophysical model is described, followed by the investigated calculation scenarios and how errors are evaluated.

2.3.1 Monte Carlo method

The interaction of particles with matter can be described by complex mathematical equations (the Boltzmann transport equations) that can be solved using two different approaches: deterministic methods and the Monte Carlo method.
Deterministic methods solve the Boltzmann transport equations directly and are computationally efficient; however, due to the complexity of these equations regarding variables such as cross-sections and geometries, they require several ap-

proximations. In other words, deterministic approaches apply exact mathematical methods to an approximated model of reality. These approximations, unfortunately, can compromise the accuracy of the final results.
Since the present work utilizes a method based on the Monte Carlo approach, a detailed description of deterministic methods is beyond the scope of this thesis.
The Monte Carlo method, conversely, estimates the solutions to complex mathematical problems using repeated random sampling. Its name derives from the city of Monte Carlo, famous for its casinos, as the core of the roulette game relies entirely on chance and probability.

Generally, a Monte Carlo simulation involves a three-step process.
The first step is the generation of a large number of random inputs; because true randomness cannot be achieved in digital computing, simulations utilize pseudo-random numbers generated via deterministic algorithms. These algorithms produce long sequences of numbers that exhibit the property of randomness based on an initial value (the seed), which guarantees the reproducibility of the results.
Second, these pseudo-random numbers are fed into the computational model to generate a single possible outcome.
Third, statistical convergence is achieved by repeating this process numerous times, and an approximation of the true physical behavior of the system is then obtained by aggregating the outcomes from all simulated histories. Because a vast number of inputs must be simulated to ensure proper convergence, the Monte Carlo method is inherently computationally demanding.

In the specific application of the Monte Carlo method to particle transport problems, the inputs represent the radiation particles, and their interactions with matter are explicitly modeled.
Initially, it is necessary to define the radiation source (including its energy spectrum and spatial distribution), alongside the geometry and material composition of the system.
For Monte Carlo transport codes, the simulation relies on some fundamental assumptions:

- each geometric region of the medium is considered homogeneous and isotropic, with material properties that are completely unaffected by particle interactions

- particles are assumed to interact exclusively with individual atoms or nuclei,

meaning that particle-particle interactions are neglected

- the transport process must be Markovian, meaning the probability of a particle interaction depends solely on its current state and not on the sequence of past events that led up to it.

Each simulation begins by retrieving a particle from the stack and transporting it through the geometry. First, the distance to the next interaction is determined. This distance is sampled from the probability distribution defined by the particle mean free path (the average distance the particle travels in the medium before interacting). At the end of each transport step, the probability distribution functions derived from the interaction cross sections are used to determine the type of interaction.
After the interaction, the final state of the particle is sampled, including its energy, direction, and any generated secondary particles. These secondary particles are added to the stack for subsequent tracking, while tracking continues for the primary particle, provided it survives the interaction and its energy remains above the cutoff value defined in the simulation parameters. At the end of each transport step, the relevant observables (e.g., energy deposition, absorbed dose, and fluence) specified in the input file are scored and accumulated throughout the simulation to provide, upon completion, an estimator of the physical quantity of interest.

The process of tracking is repeated for all the particles in the simulation, whose number must be sufficiently large to achieve statistical convergence and reach the desired statistical precision. According to statistics, indeed, increasing the number of particles by a factor of N reduces the statistical error by a factor of $\sqrt{N}$. Since computational time is proportional to the number of particles, the simulation time consequently increases by a factor of N.
While precision depends on the number of particles, the accuracy of a Monte Carlo simulation depends on the quality of the cross-section data on which the probability distribution functions are based. For this reason, it is mandatory to verify and validate radiation transport codes using experimental data or, if such data do not exist, to compare the results of one Monte Carlo transport code with another (for instance, comparing FLUKA with Geant4 or MCNP). In the context of space radiation transport, experimental data are obtained both from ground-based studies and in-flight measurements.

2.3.2 FLUKA

FLUKA (FLUktuierende KAskade) is a general-purpose tool for calculations of particle transport and interactions with matter, which can be applied to a wide range of fields, from proton and electron accelerator shielding to calorimetry, dosimetry, and neutron physics.
FLUKA can simulate a broad spectrum of particles (60 different types) across a wide energy range; for example, photons and electrons can be transported from 1 keV up to thousands of TeV, while hadrons can be simulated with energies up to 20 TeV, as reported in the FLUKA manual [34].

In this thesis, FLUKA was used to simulate, for the SPE of August 1972, the transport of space radiation and its interaction with spacecraft shielding of various thicknesses and two distinct geometries, with the aim of predicting radiation exposure in astronaut organs under different conditions.
Regarding the source term required to describe SPEs, FLUKA includes built-in files for the particle flux as a function of energy for H, He, and O ions for the events of January 20^{th}, 2005, and October 28^{th}, 2003. However, no such files are available for the August 4^{th}, 1972 event. The strategy adopted to model this specific source is explained in Section 2.3.3.
Although GCR biological effects are not investigated in this work, it is important to note that FLUKA provides dedicated files to simulate the differential energy spectra of various elements at both solar minimum and solar maximum. As explained in Section 1.1.1, solar activity modulates the GCR spectrum, resulting in a higher flux during solar minimum and a reduced flux during solar maximum. The pioneering model developed by Badhwar and O'Neil in 1992 was semi-empirical, as it was derived from fitting the measured differential flux of elements from hydrogen to nickel ($Z = 28$) outside the heliosphere as a function of energy per nucleon. For each element, the flux was described by a power law in total energy per nucleon, referred to as the Local Interstellar Spectrum (LIS). This spectrum, however, did not account for the modulation of GCRs due to solar winds, which causes a deviation from the power law particularly evident below 10 GeV/u. To incorporate this effect, a time-dependent solar modulation parameter, ϕ, was introduced. The GCR spectrum model was subsequently improved by including built-in files for solar minimum ($\phi = 456$ MV) and solar maximum ($\phi = 1440$ MV).

Furthermore, another essential feature for this work is the capability to model highly detailed geometrical models, replicating not only the spacecraft structures but also male and female anthropomorphic phantoms, including their internal organs and specific atomic compositions. FLUKA manages complex geometries through its Combinatorial Geometry package, which combines basic convex bodies (such as cylinders, spheres, and parallelepipeds) into intricate shapes using Boolean operations (union, intersection, and subtraction). Additionally, this package supports voxel , which are geometries, essential for describing human voxel phantoms. A detailed description of the male and female phantoms will be provided in Section 2.3.4.

2.3.3 Description of the August 1972 SPE

A fundamental step in a FLUKA simulation is to define the radiation source; since the August 1972 event is investigated in this work, it was necessary to model a source replicating that specific event.
The source was modeled with a spherical geometry with a 200 cm radius because the incident radiation field can be assumed to be isotropic, as isotropy is usually achieved relatively quickly after an SPE begins.
Regarding the types of particles composing the event, although the vast majority of primary particles are protons, heavier ions cannot be neglected due to their significant impact on biological effects. Specifically, in addition to protons, helium and oxygen ions were considered.
Concerning protons, their energy fluence spectrum was obtained from Eq. 2.14, which was developed by the NASA Langley Research Center (LaRC) through the fitting of satellite data [35].

$$\frac{d\phi_p(E)}{dE} = 2.20 \times 10^7 e^{-\frac{E-100}{30}} \tag{2.14}$$

with the proton differential fluence $\frac{d\phi_p(E)}{dE}$ expressed in $cm^{-2}MeV^{-1}$ and the kinetic energy E in MeV. Integrating Eq. 2.14 in energy, the proton integral fluence $\phi(> E)$ is equal to:

$$\phi(> E) = 6.60 \times 10^8 e^{-\frac{E-100}{30}} \tag{2.15}$$

with proton integral fluence expressed in cm^{-2} and the kinetic energy E in MeV. Concerning Helium and Oxygen, their spectra was based on measurement taken during a rocket flight conducted as part of the SPICE (Solar Particle Intensity and Composition Experiment) program as reported in [36] and both spectra are

fitted with the function

$$e^{-\frac{E}{E_0}} \tag{2.16}$$

where E_0 is 16.3 MeV/u for He and 12.0 MeV/u for O.
The particle differential flux for this event is shown in Fig. 2.2 and it is implemented as a source in the simulation.

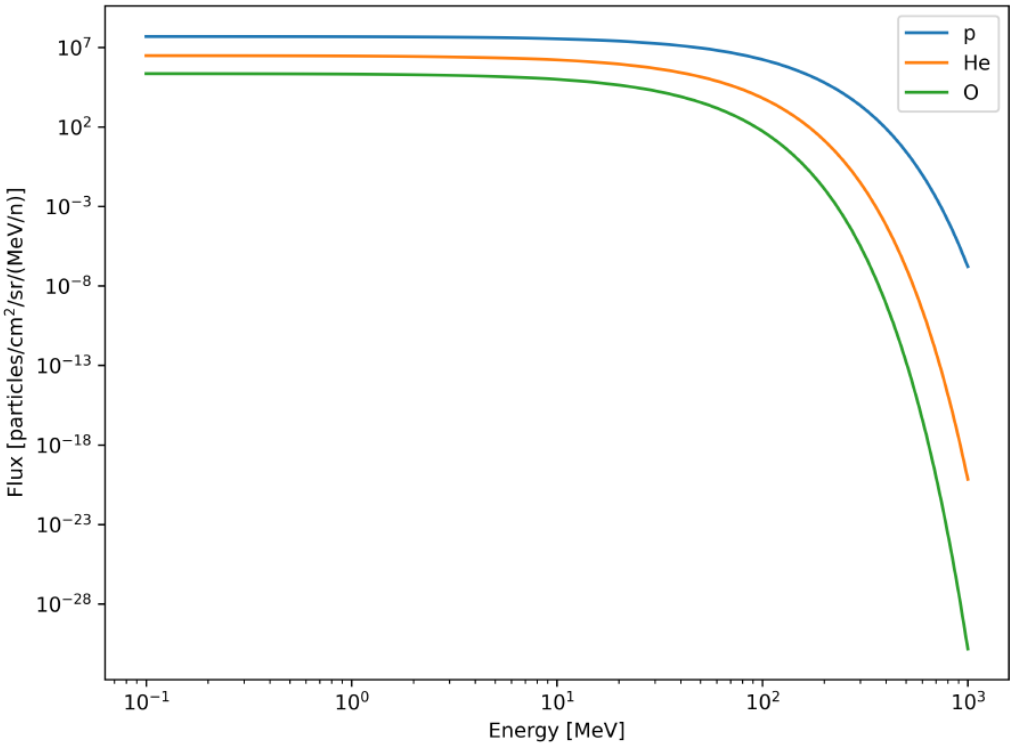

Figure 2.2: Particle differential flux for the August 1972 SPE

2.3.4 Anthropomorphic phantoms (male and female)

The development of computational phantoms (or mathematical models) plays a crucial role in radiation dosimetry, as they are used to evaluate energy deposition in various organs resulting from both internal and external exposures.
Traditionally, anatomical phantoms were constructed using analytical mathematical expressions to represent geometric shapes (such as planes, cylinders, ellipses, and spheres) to approximate the shape and position of idealized body organs. This type of phantom was originally developed for the Medical Internal Radiation Dose (MIRD) Committee of the Society of Nuclear Medicine at the Oak Ridge National Laboratory. Based on the original adult MIRD phantom, several

pediatric phantoms of various ages were subsequently modeled, alongside separate male and female models named "Adam" and "Eva". Finally, four models were developed to represent the adult female when non-pregnant, as well as at three distinct stages of pregnancy.

During the last two decades, these MIRD models have been significantly improved and have evolved into a new type of anatomical phantom called tomographic or voxel models. They provide a much more realistic replication of the human body being based on high-resolution medical scans (e.g., computed tomography or magnetic resonance imaging) of a single individual. Voxel models are formed by a large number of volume elements (voxels). Although they offer the most detailed representation of human anatomy currently available, because they are derived from a specific individual, they do not necessarily represent the reference adult male or female. For this reason, the International Commission on Radiological Protection (ICRP) adopted the Reference Male and Reference Female phantoms; these models are based on real medical imaging data but are adjusted to be fully consistent with the reference anatomical and physiological parameters described in ICRP Publication 89 [37].

The starting point for constructing the adult Reference Male and Reference Female voxel phantoms was the acquisition of tomographic datasets from individuals whose external dimensions were close to the official reference values, thereby minimizing the modifications required to match the reference cases.
For the male phantom, the real imaging data were obtained from whole-body CT scans of a 38-year-old leukemia patient who was 176 cm tall and weighed slightly less than 70 kg, dimensions close to the reference standards of 176 cm and 73 kg. Correspondingly, the female phantom was constructed based on a 43-year-old patient with a height of 168 cm and a weight of 59 kg, which was similar to the standard reference dimensions of 163 cm and 60 kg.
The initial male digital model was designated as *Golem*, while the female model was named *Laura*.
Both phantoms are segmented and discretized into volume elements (voxels). Each voxel is assigned a specific identification number (ID) that links it to a particular organ or tissue. In this manner, each anatomical structure is defined by a collection of voxels sharing the same ID number. The organs and tissues described in these models are those most relevant for radiation protection purposes, commonly referred to as *target regions*. They include: active bone mar-

row, adrenals, brain, breast, colon, endosteal tissue (formerly referred to as bone surfaces), extrathoracic airways, eyes, gall bladder, heart, kidneys, liver, lungs, lymphatic nodes, muscle, esophagus, oral mucosa, ovaries, pancreas, prostate, salivary glands, skin, small intestine, spleen, stomach, testes, thymus, thyroid, urinary bladder, and uterus.

As previously mentioned, the *Golem* and *Laura* models had to undergo several modifications, either to the body as a whole or to specific organs, to accurately fit the ICRP reference parameters. These modifications included:

- Adjustment of the body height and the skeleton mass of the segmented model to the reference data by voxel scaling
- Adjusting of individual organ masses to the target values by adding or removing voxels corresponding to those specific structures.
- Addition of tissues not present in the segmented phantoms or sub-division of larger entities (such as skeleton and gastro-intestinal track)
- Adjustment of the whole body mass to the reference values by adding or subtracting a respective number of adipose tissue voxels

Finally, the Reference Female and Male phantoms were successfully modeled. Their geometries were visualized using Flair, an advanced user-friendly interface for FLUKA designed to facilitate input file editing, code execution, and geometry visualization. Both coronal and sagittal views of the two phantoms are presented in Fig. 2.3, while their main characteristics are summarized in Table 2.2.

Property	Male	Female
Height (m)	1.76	1.63
Mass (kg)	73.0	60.0
Number of tissue voxels	1 946 375	3 886 020
Slice thickness (voxel height, mm)	8.0	4.84
Voxel in-plane resolution (mm)	2 137	1 775
Voxel volunme (mm^2)	36.54	15.25
Number of columns	254	299
Number of rows	127	137
Number of slices	220	346

Table 2.2: Main characteristic of the adult Reference Male and Reference Female computational phantoms according with ICRP Publication 110 [38].

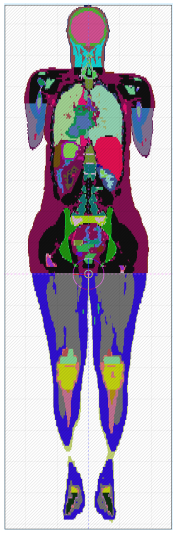

(a) Female phantom coronal view

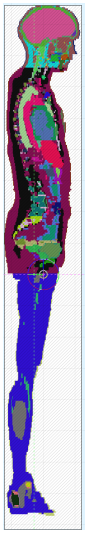

(b) Female phantom sagittal view

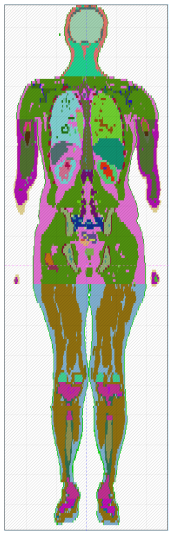

(c) Male phantom coronal view

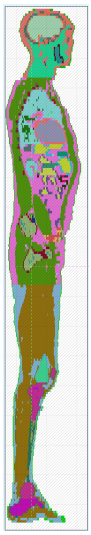

(d) Male phantom sagittal view

Figure 2.3: Coronal and sagittal cross-sections of the adults Reference Female and Male computational phantoms

2.3.5 FLUKA-BIANCA interface

At this stage, it is necessary to describe the interaction between the BIANCA model and FLUKA, detailing how the biological components of BIANCA interface with the Monte Carlo transport simulations. The interface between FLUKA and the BIANCA biophysical code enables the calculation of various radiobiological endpoints, such as the RBE for cell survival (associated with non-cancer effects) and chromosomal aberrations (associated with stochastic effects).
A key consideration when dealing with space radiation is its nature as a mixed radiation field, where various particle types and energies simultaneously contribute to both the total absorbed dose and the overall biological damage.
Consequently, the calculation of the RBE proceeds as follows. During the transport simulation, FLUKA tracks every primary and secondary particle through the geometry. At each tracking step, the code records three key quantities: the voxel where the energy deposition occurs, the Linear Energy Transfer (LET) value of the current particle, and the dose D_i deposited by that specific particle within that voxel. Based on the particle type and its specific LET, the pre-calculated BIANCA look-up tables are queried to determine the corresponding α_i and β_i coefficients.

At the end of the simulation, FLUKA computes the dose-weighted average values of α and β for each voxel, which are representative of the local mixed radiation field. These coefficients are calculated using Equations 2.17 and 2.18:

$$\alpha = \frac{\sum_{i=1}^{N} \alpha_i D_i}{\sum_{i=1}^{N} D_i} \tag{2.17}$$

$$\beta = \left(\frac{\sum_{i=1}^{N} \sqrt{\beta_i} D_i}{\sum_{i=1}^{N} D_i} \right)^2 \tag{2.18}$$

where the index i denotes the specific component of the radiation field (i.e., a particle of a given type and energy, and thus a specific LET).

Once the average α and β coefficients have been determined, the cell survival fraction S resulting from the total absorbed dose D deposited by the mixed field is equated to the survival fraction associated with a reference photon dose D_x required to produce the same biological effect:

$$S = e^{-(\alpha D + \beta D^2)} = e^{-(\alpha_x D_x + \beta_x D_x^2)} \tag{2.19}$$

$$\Downarrow$$

$$\alpha D + \beta D^2 = \alpha_x D_x + \beta_x D_x^2 \tag{2.20}$$

In this manner, D_x can be analytically solved via the quadratic formula as:

$$D_x = \frac{-\alpha_x + \sqrt{\alpha_x^2 + 4\beta_x(\alpha D + \beta D^2)}}{2\beta_x} \tag{2.21}$$

Finally, the Relative Biological Effectiveness (RBE) is obtained according to its standard definition (Eq. 1.14):

$$\text{RBE} = \frac{D_x}{D} \tag{2.22}$$

2.3.6 Calculation scenarios

This section describes the characteristics of the simulations implemented in FLUKA, focusing on the phantoms employed, the shielding scenarios, the radiation source, and the quantities evaluated.

Simulated geometries

The simulated configurations incorporated both male and female phantoms, since the distinct anatomical characteristics of the two sexes directly influenced the values of the investigated quantities.
These phantoms were modeled within a shielding layer designed to simulate the protective environment surrounding an astronaut's body. Two distinct shielding configurations were considered: spherical and cylindrical. The cylindrical geometry was selected in line with previous studies, whereas the spherical geometry was included because it is commonly adopted as a reference geometry in space radiation shielding studies.

To represent the different scenarios encountered by astronauts, various shielding thicknesses were evaluated. The minimum thickness investigated was 0.3 g/cm^2, which represents the worst-case scenario in case of extravehicular activity (EVA) with a light spacesuit, whereas the maximum thickness 35 g/cm^2, corresponding to the more heavily shielded spacecraft areas where astronauts take refuge upon notification of an intense Solar Particle Event (SPE). Note that the thickness is expressed in terms of areal density (g/cm^2), as is standard practice in radiation

physics. The areal density is defined as the product of the physical thickness and the material density, since the energy loss per unit areal density (mass stopping power) is independent of the material physical density.

A visual example of the shielding configuration is shown in Fig. 2.4, which displays the coronal views of the male phantom inside cylindrical and spherical aluminum shields with a thickness of 5 g/cm^2.

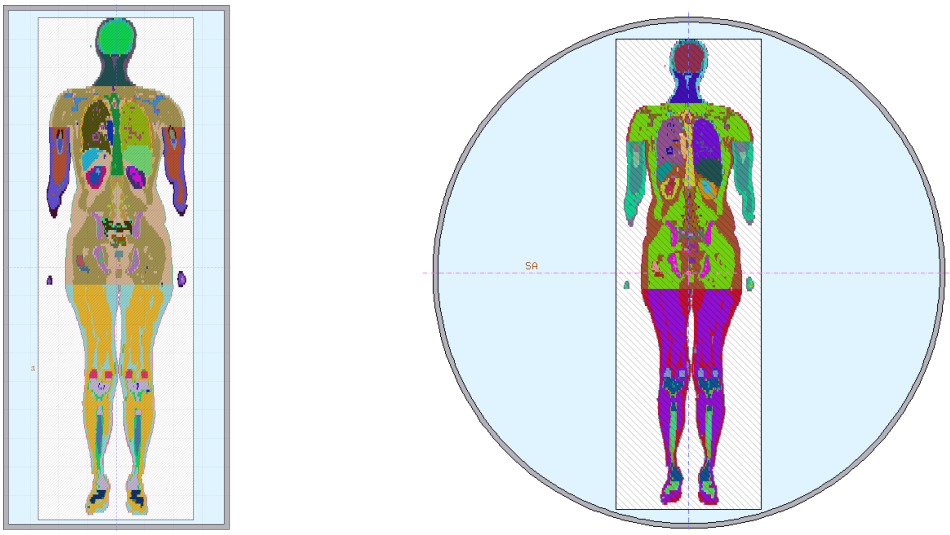

(a) Male phantom in cylindrical shield of 5 g/cm^2

(b) Male phantom in spherical shield of 5 g/cm^2

Figure 2.4: Male phantoms in cylindrical and spherical shield

Radiation source

The primary radiation source investigated in this work was the historical Solar Particle Event (SPE) of August 1972. Specific spectral properties and physical characteristics of this event are comprehensively detailed in Section 2.3.3.

Investigated quantities

The quantities investigated in this study included the absorbed dose to the skin for both the male and female phantoms, and to the breast for the female phantom.

To account for the biological response, previous studies typically used the fibroblast cell line as a reference for all organs of the human body. Conversely, this thesis introduces the use of HaCaT and MCF10A cell lines specifically for the skin and breast, respectively. The widespread use of fibroblasts in past literature stems from the extensive availability of cell survival data compared to other

human cell types. Furthermore, since fibroblasts contribute to the formation of connective tissue, they are found in virtually every part of the human body.

However, modeling all human organs using exclusively fibroblasts represents a significant oversimplification and a proper distinction between different tissue-specific cell lines is necessary. Therefore, in this work, the radiation response in skin and breast tissues was evaluated using both the fibroblast and HaCaT or MCF10A cell lines. The resulting RBE-weighted doses were then calculated to provide a direct comparison of the predicted radiation effects between these models.

Finally, to evaluate the impact of dose protraction, since the August 1972 event spanned several hours, the Lea-Catcheside factor is implemented. The RBE-weighted dose is assessed across various exposure durations ranging from 2 to 16 hours, and the relative difference between modeling the event as instantaneous versus protracted over 16 hours is discussed.

2.3.7 Statistical error

As a Monte Carlo radiation transport code, FLUKA is characterized by an intrinsic statistical uncertainty that depends on the number of simulated particles and runs. Consequently, increasing both the number of particles per simulation (n_i) and the total number of simulations (N) directly enhances the statistical precision of the output.

In this work, the number of simulated runs was set to 5 while the number of simulated particles increases with increasing shielding thickness, ranging from 3×10^6 up to 2×10^8 for the 35 g/cm^2 configuration. This scaling of primary particles is necessary to counteract the shielding attenuation; as thickness increases, a larger fraction of particles undergoes interactions within the shield, meaning fewer of them reach the organs of interest. With this allocation of primary histories, the statistical error associated with both the absorbed dose and the RBE-weighted absorbed dose results is always less than 2% for both the skin and the breast.

Concerning the statistical quantities and their associated errors, the formal definitions are described below.

The *sample mean* of the data obtained by executing N independent runs is defined as:

$$\langle Y \rangle = \frac{1}{N} \sum_{i=1}^{N} Y_i \tag{2.23}$$

where Y_i is the output of the i-th run.

The *sample variance*, which quantifies the dispersion of the individual outputs

around the mean value, is given by:

$$S^2 = \frac{1}{N-1} \sum_{i=1}^{N} (Y_i - \langle Y \rangle)^2 \tag{2.24}$$

FLUKA directly calculates the sample variance using the following mathematically equivalent formula weighted by history numbers:

$$S^2 = \frac{1}{N-1} \left[\frac{\sum_{i=1}^{N} n_i Y_i^2}{n} - \left(\frac{\sum_{i=1}^{N} n_i Y_i}{n} \right)^2 \right] \tag{2.25}$$

where $n = \sum_{i=1}^{N} n_i$ represents the total number of histories accumulated across the N runs.

The *sample standard deviation* is computed as the square root of the variance:

$$S = \sqrt{S^2} \tag{2.26}$$

The *standard error of the mean* (SE), which provides an estimate of the uncertainty of the calculated mean and represents the error associated with the reported values, is defined as:

$$SE = \frac{S}{\sqrt{N}} \tag{2.27}$$

The *relative standard error* (RSE) is usually expressed as a percentage and allows for a direct comparison of the precision achieved across different simulation configurations:

$$RSE = \frac{SE}{\langle Y \rangle} \tag{2.28}$$

CHAPTER 3

Results

This chapter presents the results obtained in this work together with their discussion.
The first part focuses on the generation of the cell-specific radiobiological databases using the BIANCA model. This includes the characterization of the photon response, the validation of the model predictions for ion irradiation against the available experimental data, and the comparison of the resulting databases.
The second part of this chapter applies these databases to investigate the radiation effects associated with the August 1972 Solar Particle Event (SPE), one of the most intense SPEs on record. Male and female computational phantoms are used to simulate astronauts sheltered inside cylindrical and spherical structures. Since the available databases correspond to skin and breast cell lines, the analysis focuses on these two tissues. First, the physical absorbed dose is evaluated, followed by the RBE-weighted absorbed dose predicted by the two databases. Finally, the influence of the Lea-Catcheside factor is investigated to assess the impact of the temporal profile of the SPE on sublethal damage repair.

3.1 Generation of cell-specific databases with BIANCA

The generation of the cell-specific databases, consisting of the α and β parameters of the linear-quadratic model for various ions as a function of LET, represented the first step of this work. The databases were generated using the BIANCA model by

first characterizing the photon response of each cell line, then validating the model predictions for ion irradiation against the available experimental data, and finally deriving the corresponding LET-dependent radiobiological parameters. Finally, the resulting α and β parameters were compared to investigate the differences among the considered cell lines.

3.1.1 Photon response characterization using BIANCA

As described in Section 2.2, cell-specific radiobiological databases were developed for the HaCaT and MCF10A cell lines. In addition, the previously available fibroblast database was updated, resulting in a new version that was used throughout this work. The updated fibroblast database was obtained by performing a new set of BIANCA simulations and re-evaluating the corresponding α and β parameters. For the HaCaT and MCF10A cell lines, the first step was to determine the CL and f parameters for photon irradiation. To this end, a literature search was conducted to identify studies reporting clonogenic survival data for these cell lines following photon irradiation.

For the HaCaT cell line, the available studies included irradiations with 200 kVp X-rays [39] and 6 MV photon beams [40, 41]. The corresponding clonogenic survival curves as a function of dose are shown in Figure 3.1, where the black curve represents irradiation with 200 kVp X-rays and the red curves correspond to 6 MV photon irradiation.

MCF10A cells were irradiated with ^{137}Cs γ-rays in [42, 43], with ^{60}Co γ-rays in [44], and with 6 MV photons in [40, 45]. The corresponding clonogenic cell survival as a function of dose is shown in Figure 3.2, where the blue curves represent irradiation with ^{137}Cs γ-rays, the brown curve irradiation with ^{60}Co γ-rays and the green curves represent irradiation with 6 MV photons. For reference, the γ-ray energy emitted by ^{137}Cs is 662 keV, whereas ^{60}Co emits two principal γ-rays with energies of 1.17 and 1.33 MeV.

Despite the variability among the different studies, an overall trend can be observed in which both cell lines exhibit a lower survival fraction at lower photon energies, whereas survival increases with increasing photon energy, becoming particularly evident at 6 MV. This behavior is consistent with the decrease in LET as photon energy increases.

Another key observation concerns the behavior of the same cell line irradiated with photons of the same energy but investigated in different studies. For example, as shown in Figure 3.1, HaCaT cells irradiated with 6 MV photons from references [40] and [41] (red curves) display two distinct survival curves. A similar

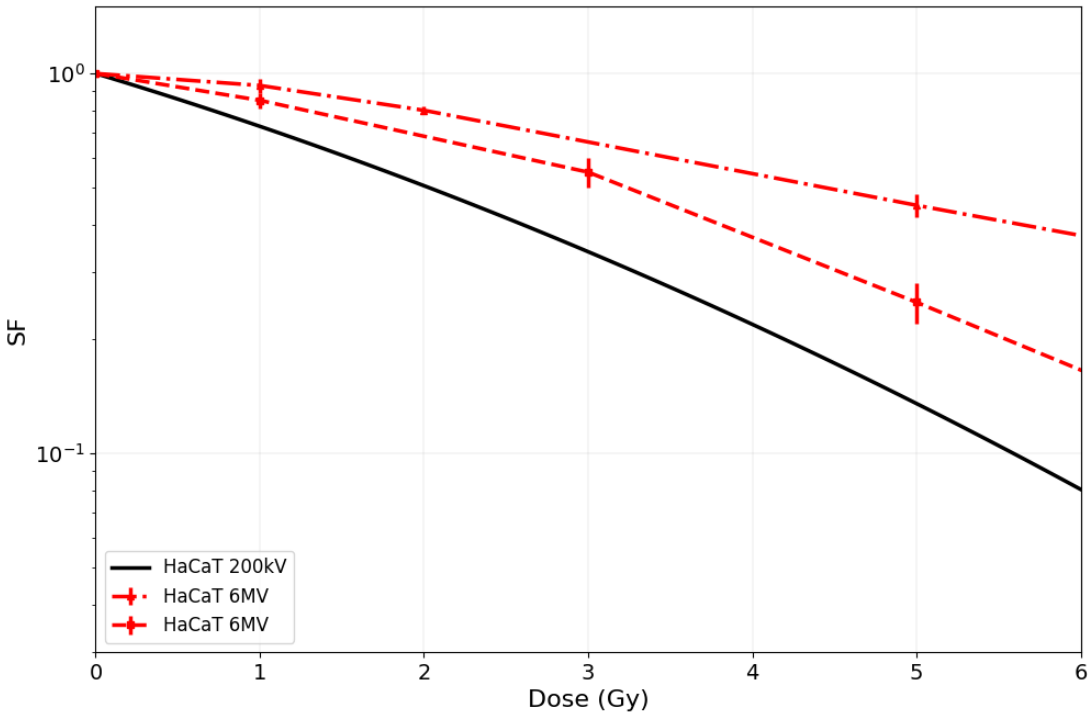

Figure 3.1: Survival fraction (SF) as a function of dose for HaCaT cells irradiated with 200 kVp X-rays ([39] black line) and 6 MV (red lines, dashdot [40] and dashed [41])

discrepancy is observed for MCF10A cells irradiated with 6 MV photons in Figure 3.2 (green curves). These differences can be attributed to inter-laboratory variations, including differences in cell culture conditions, passage number, irradiation setup, and clonogenic assay protocols.

The next objective was to compare the responses of the HaCaT and MCF10A cell lines following photon irradiation to verify whether their photon response can be considered equivalent. If this hypothesis holds true, it would be possible to define a single set of CL and f parameters for both cell lines. Consequently, these shared parameters could be applied to both photon and ion irradiations at a specific LET value, allowing the model predictions to be validated against the experimental data from both cell lines. This approach is particularly advantageous because experimental data for HaCaT and MCF10A cell lines after ion irradiation are currently scarce; thus, pooling the available data provides a sufficient number of experimental points to properly validate the model.

The comparison between the clonogenic survival curves of both cell lines is shown in Figure 3.3.

As shown in Figure 3.3, the HaCaT and MCF10A cell lines exhibit a similar behavior. This similarity is observed both for low-energy photon irradiations in

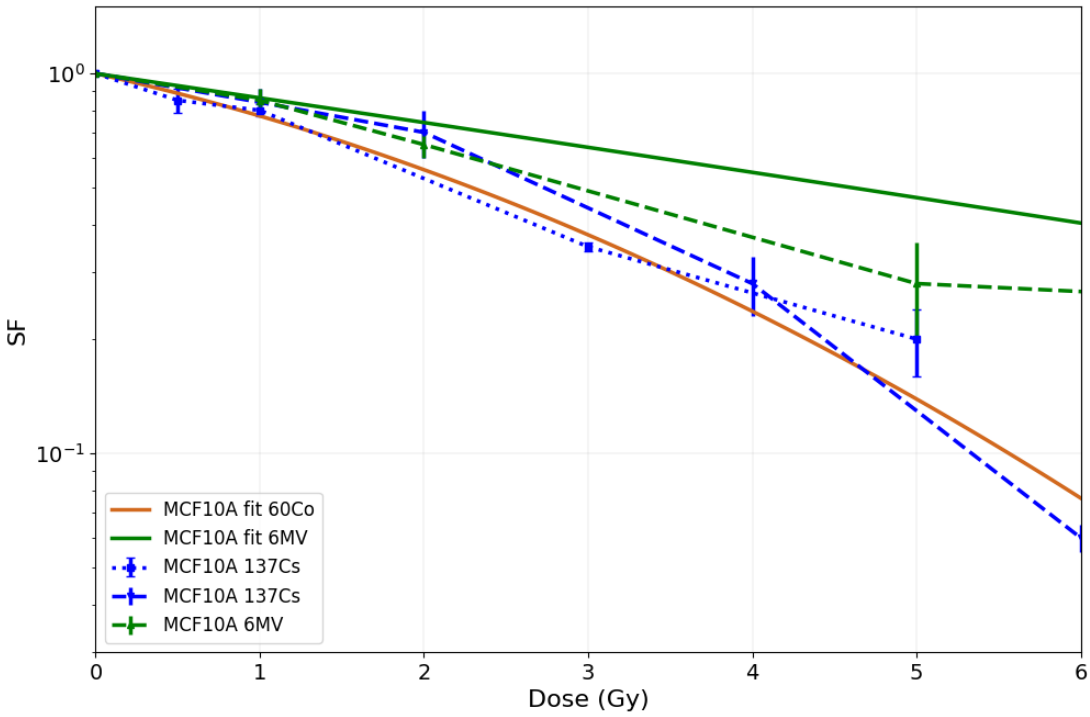

Figure 3.2: Survival fraction (SF) as a function of dose for MCF10A cells irradiated with ^{137}Cs γ-ray (blue lines, dotted [42], dashed [43]), with ^{60}Co γ-rays (brown line, [44]) and with 6MV photons (green lines, solid [45], dashed [40]).

Fig. 3.3a, when comparing 200 kVp X-rays for HaCaT (black curve) with ^{137}Cs γ-rays (blue curves) and with ^{60}Co γ-rays (brown curve) for MCF10A , and for 6 MV photon irradiation in Fig. 3.3b (red curves for HaCaT and green curves for MCF10A). The survival curves obtained with ^{137}Cs and ^{60}Co are also highly consistent, despite their different photon energies, indicating that the biological response is essentially unaffected by these relatively small energy differences.

The hypothesis of an equivalent photon response is also supported by biological considerations, since both HaCaT and MCF10A are epithelial cell lines. Specifically, HaCaT cells are derived from human skin (keratinocytes), whereas MCF10A cells originate from mammary tissue.

Throughout the remainder of this work, HaCaT and MCF10A were therefore assumed to share the same photon response and are described using a common set of CL and f parameters. This assumption enables the available experimental data from both cell lines to be combined, providing a sufficient number of ion irradiation data points for a robust validation of the BIANCA model.

The next step involved determining the CL and f parameters for these cell lines following photon irradiation. Consequently, it was necessary to select which of the survival curves shown in Figure 3.3 would serve as the reference for this

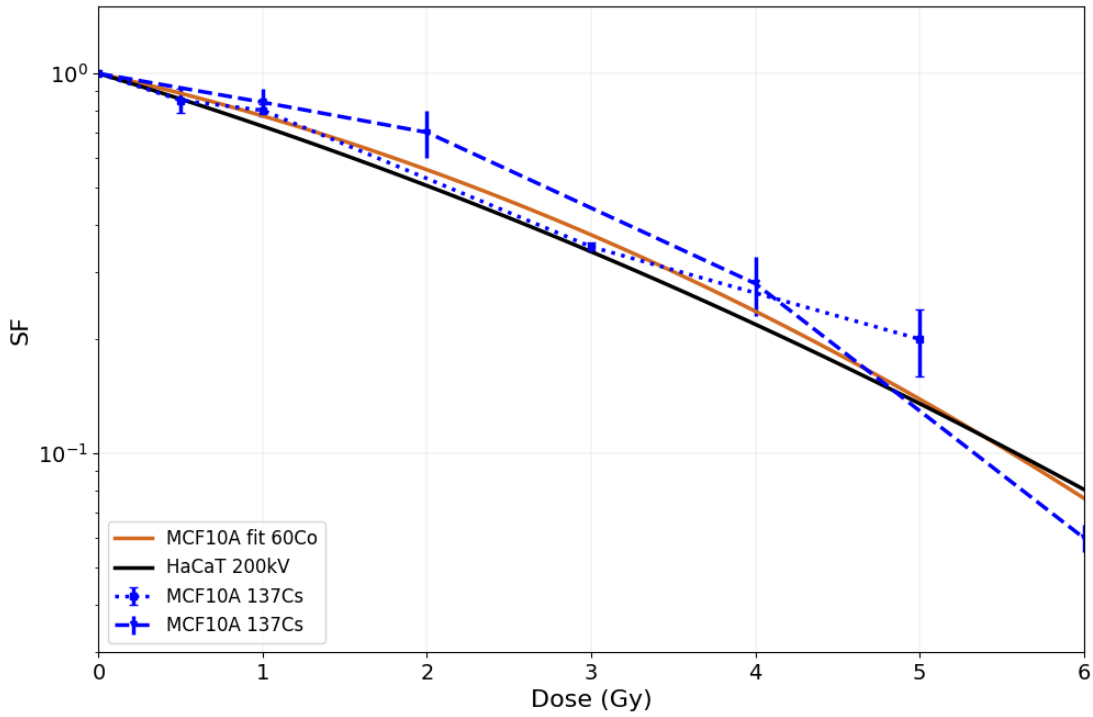

(a) Irradiation with photons of 200 kV, ^{137}Cs and ^{60}Co

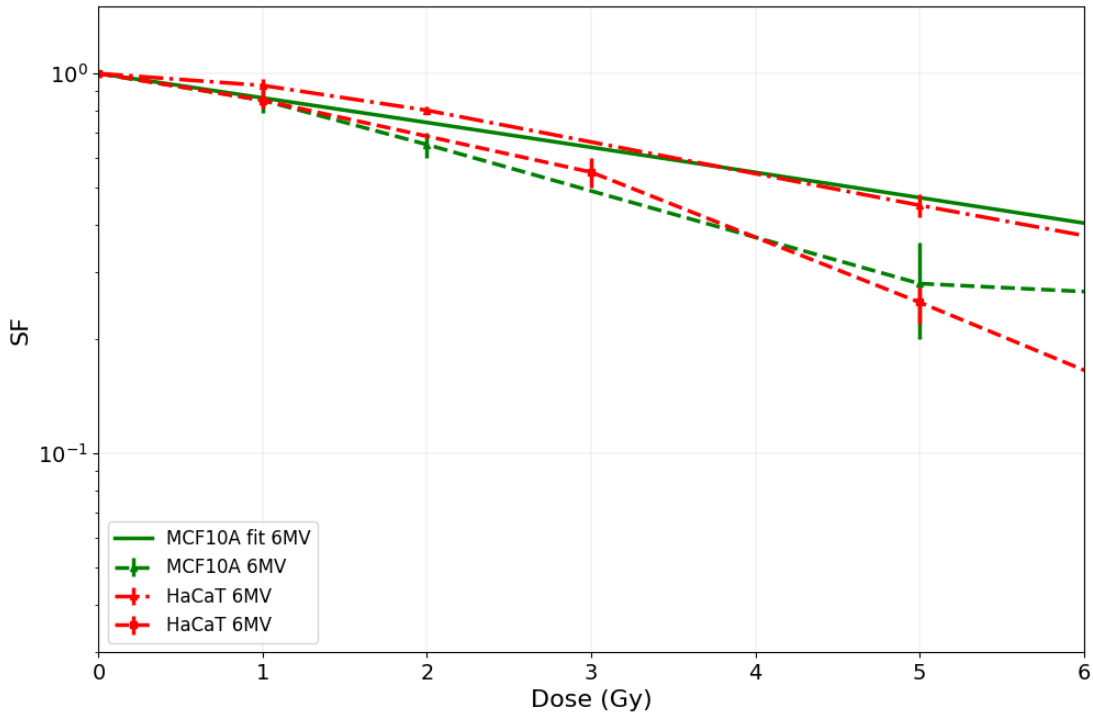

(b) Irradiation with photons of 6MV

Figure 3.3: Survival fraction (SF) as a function of dose for HACAT and MCF10A cells. Data points were taken from [39–45].

parameter evaluation. The data for HaCaT cells irradiated with 200 kVp X-rays (black curve) from [39] were selected. This choice was motivated by the fact that the same study also included proton irradiation data, thereby facilitating the subsequent comparison between the model predictions and the experimental results for ion irradiation.

To determine the optimal CL and f parameters that best fitted the experimental data from [39], a series of BIANCA simulations was performed. The final optimized values were $CL = 1.2\ CL \cdot Gy^{-1} \cdot cell^{-1}$ and $f = 0.26$. This parameter set produced a simulated survival curve with $\alpha = (0.312 \pm 0.006)$ Gy^{-1} and $\beta = (0.018 \pm 0.002)$ Gy^{-2}, which is in agreement with the experimental values reported in the study $\alpha_{\text{exp}} = (0.30 \pm 0.03)$ Gy^{-1} and $\beta_{\text{exp}} = (0.02 \pm 0.01)$ Gy^{-2}. The comparison between the experimental and simulated survival curves is shown in Figure 3.4.

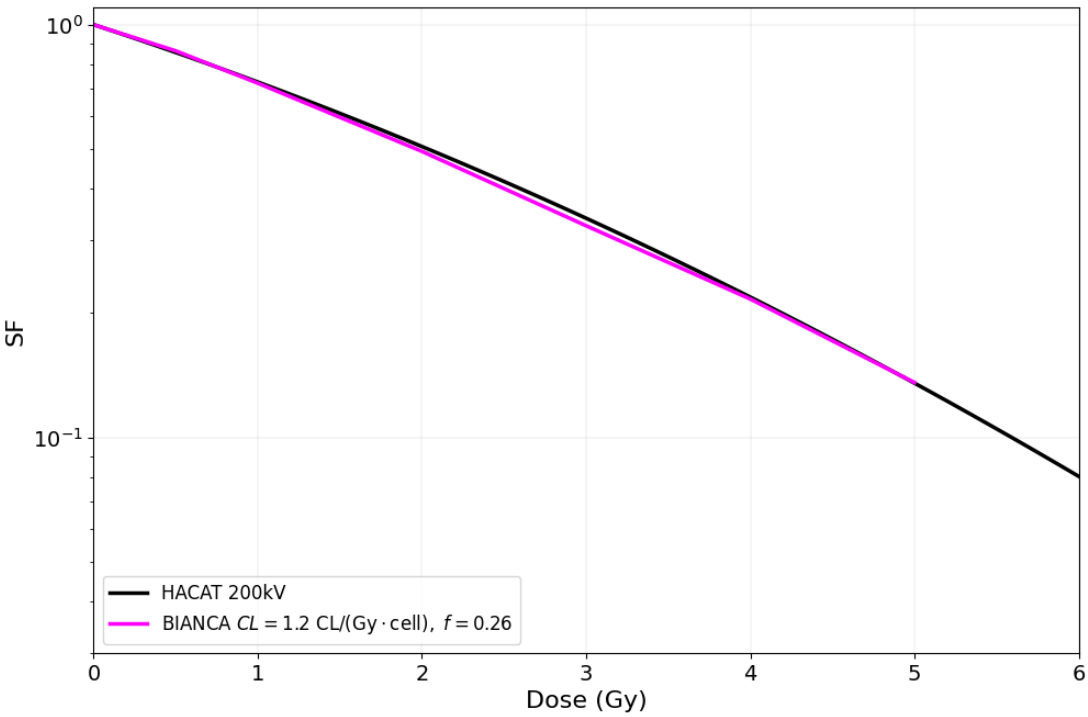

Figure 3.4: Comparison between the experimental reference curve for HaCaT cells after photon irradiation from [39] (black curve) and the optimized BIANCA simulation curve (magenta curve).

Once the CL and f parameters for photon irradiation of the HaCaT/MCF10A cell lines had been determined, Equations 2.12 and 2.13 were applied to calculate the corresponding parameters for each ion species at a given LET.

3.1.2 Radiobiological database validation

Before constructing the radiobiological database, validation of the BIANCA model was a fundamental step. To this end, experimental data for ion-irradiated HaCaT and MCF10A cells were collected from previous studies.

Specifically, the data were obtained from [39], in which HaCaT cells were irradiated with protons at six different LET values (1.9, 2.1, 2.5, 2.8, 4.5 $keV/\mu m$); from [46], in which MCF10A cells were irradiated with protons at a single LET value (5 $keV/\mu m$); and from [41], in which HaCaT cells were irradiated with carbon ions at an LET value equal to 30 $keV/\mu m$. The comparison between the experimental data and the BIANCA model predictions is shown in Figure 3.5.

The BIANCA model successfully reproduced the experimental data. Specifically, under proton irradiation (Figs. 3.5a, 3.5b, and 3.5c), the model predictions consistently fell within the experimental error bars. Under carbon ion irradiation (Fig. 3.5d), the simulated survival curve was in good agreement with the experimental data. It is worth noting that, in Fig. 3.5d, the experimental survival fraction measured at 3 Gy appears to be unexpectedly high for that specific dose level. Nevertheless, the BIANCA model accurately reproduces the overall trend of the experimental data.

3.1.3 Radiobiological database generation

Once the BIANCA model had been validated using the parameters $CL = 1.2$ $CL \cdot Gy^{-1} \cdot cell^{-1}$ and $f = 0.26$ for photons, the radiobiological database was constructed.

Since the direct output of the BIANCA model consists of survival fraction values as a function of dose, these data were fitted using the linear-quadratic model (Eq. 2.3) to derive the α and β parameters for each ion species at different LET values.

As described in Section 2.1.3, the ions were grouped according to their atomic number (Z) into five categories: protons ($Z = 1$), Helium and Lithium ions ($Z = 2$–3), ions with atomic number $4 \leq Z \leq 8$, ions with $9 \leq Z \leq 14$, and ions with $Z \geq 15$. For each category, a specific set of LET values was selected to account for the different physical characteristics of the particles.

The resulting α and β parameters for HaCaT and MCF10A cells are shown as a function of LET in Fig. 3.6, with the associated uncertainties derived from the linear-quadratic (LQ) model fit.

As shown in Fig. 3.6, the α coefficient initially increases with LET, reaches a

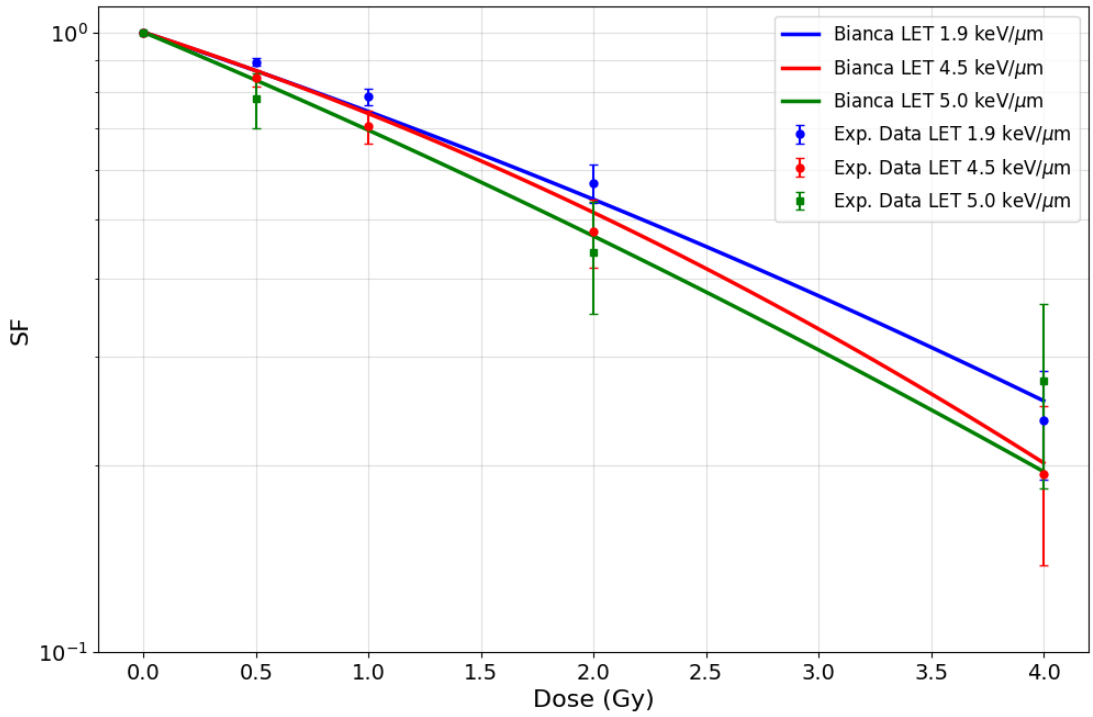

(a)

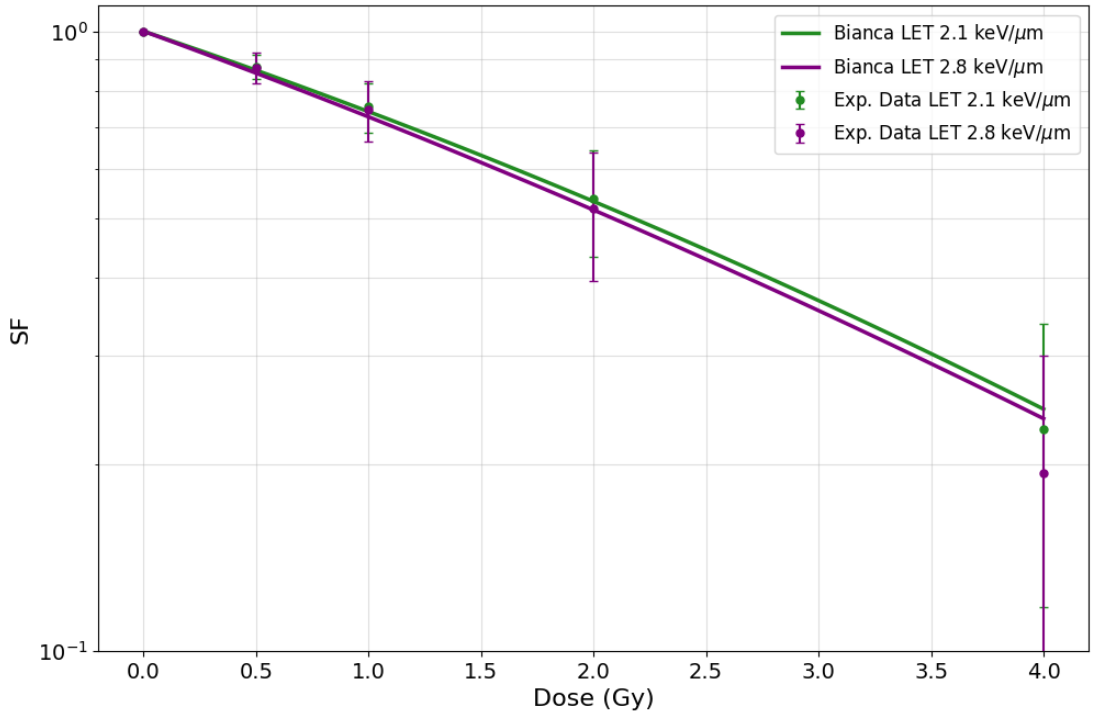

(b)

Figure 3.5: Comparison of experimental data for proton beams

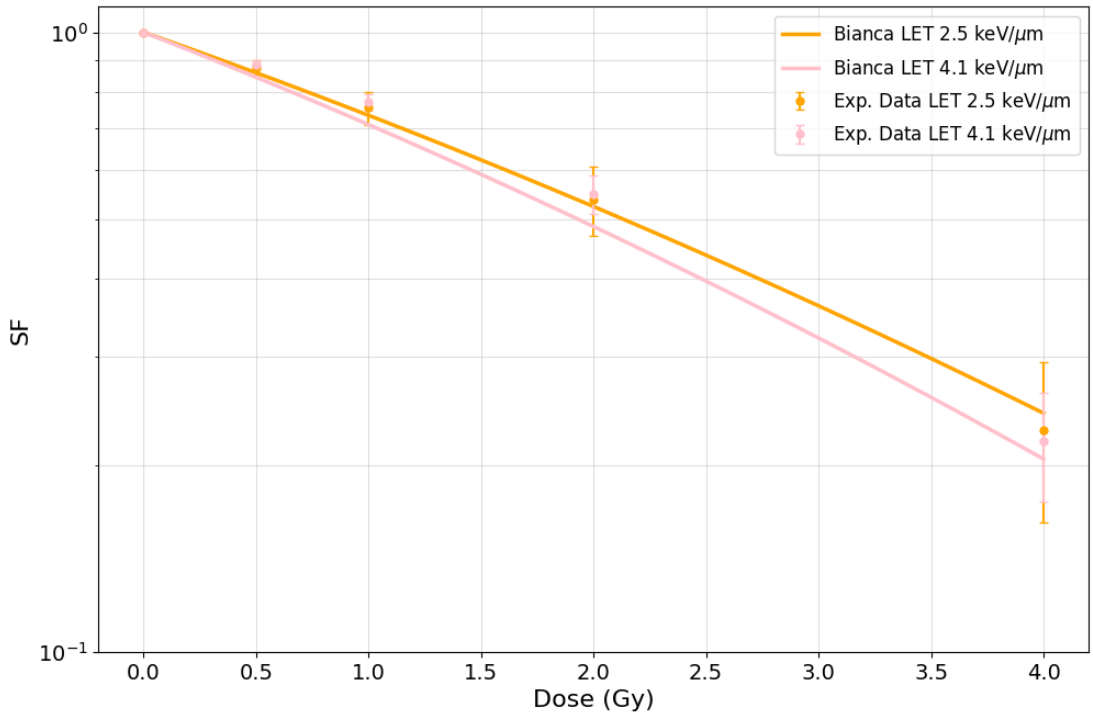

(c)

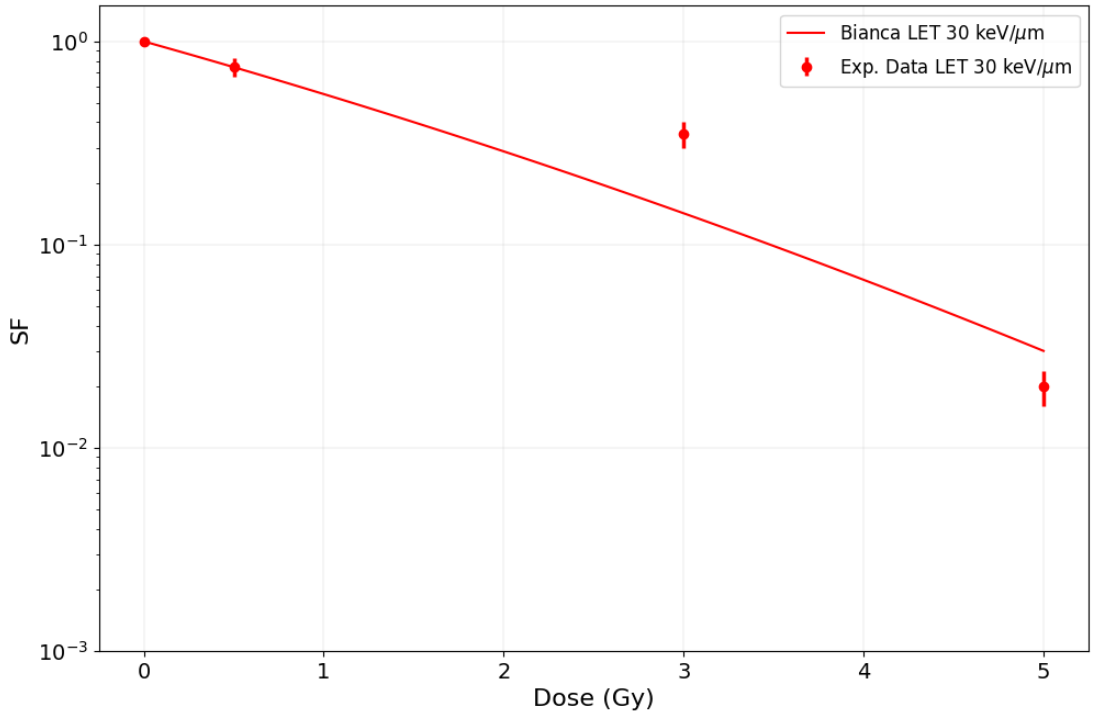

(d)

Figure 3.5: Comparison of experimental data for proton and carbon ion beams

maximum, and subsequently decreases. This characteristic behaviour is observed for heavy ions but not for protons and is associated with the so-called *overkill effect*. At very high LET values, the energy deposited within the cell becomes so concentrated that additional energy deposition does not produce a proportional increase in biological damage. Consequently, part of the deposited energy does not contribute to further cell inactivation, leading to a reduction in biological effectiveness.

In contrast, the β parameter does not exhibit a well-defined dependence on LET, showing considerable scatter over the investigated LET range. For ions with $Z = 2$–3 and ions with $4 \leq Z \leq 8$, the β parameter was fixed to zero for LET values above 100 keV/μm and 175 keV/μm, respectively. This decision was based on the observation that, at high LET, the linear-quadratic fits of the BIANCA-predicted survival fractions yielded β values that were statistically consistent with zero within their uncertainties, fluctuating between small positive and negative values. Since negative β values have no physical or biological meaning, setting $\beta = 0$ represents the most robust and widely accepted approach.

The resulting database therefore provides LET-dependent radiobiological parameters for all the considered ion species and constitutes the basis for the biological dose calculations presented in the following sections. These parameters can be directly coupled with particle transport simulations to estimate the biological effectiveness of complex mixed radiation fields.

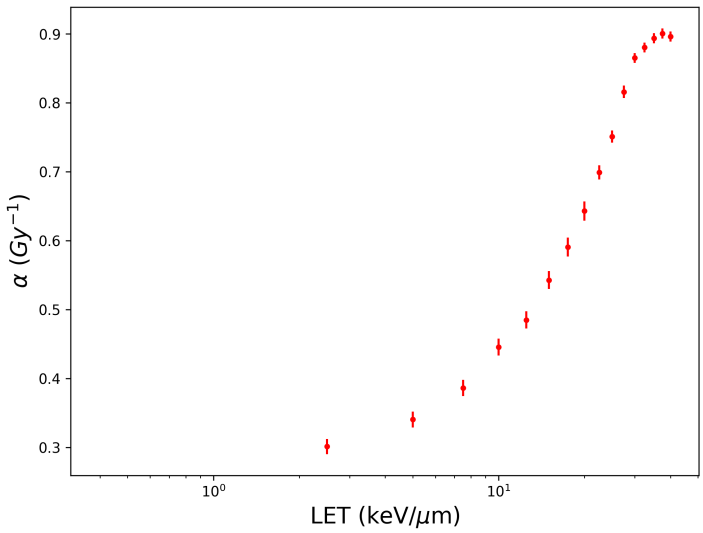

(a) α values for ions with $Z = 1$

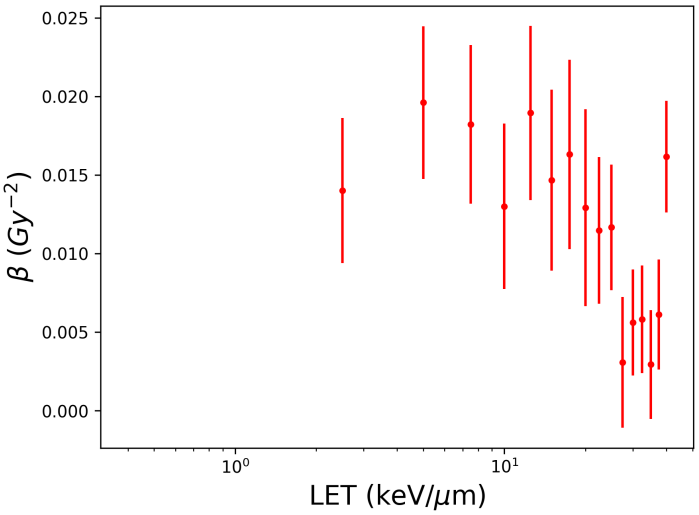

(b) β values for ions with Z=1

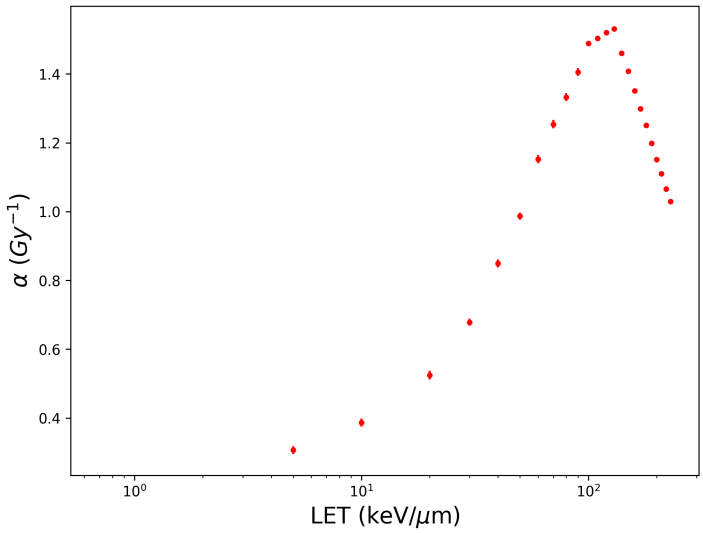

(c) α values for ions with $Z = 2$–3

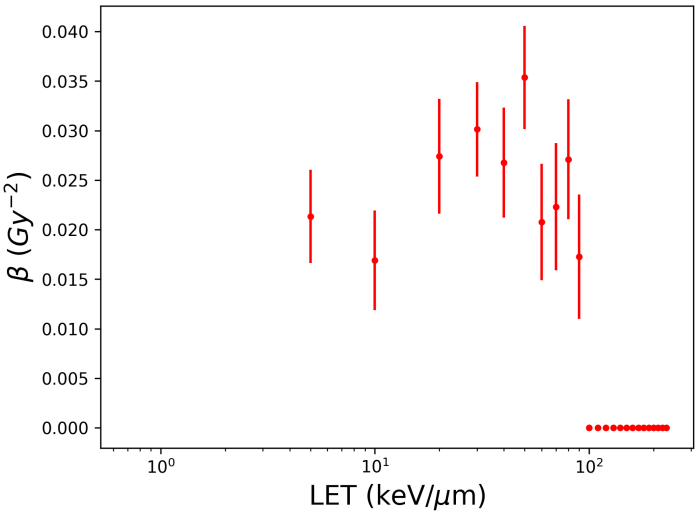

(d) β values for ions with $Z = 2$–3

Figure 3.6: α and β values for HaCaT and MCF10A for ions with $Z = 1$ and $Z = 2 - 3$ at various LET.

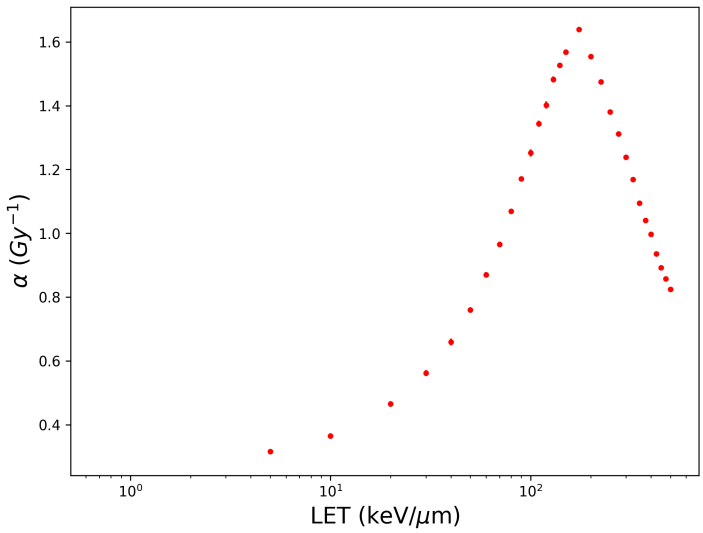

(e) α values for ions with $4 \leq Z \leq 8$

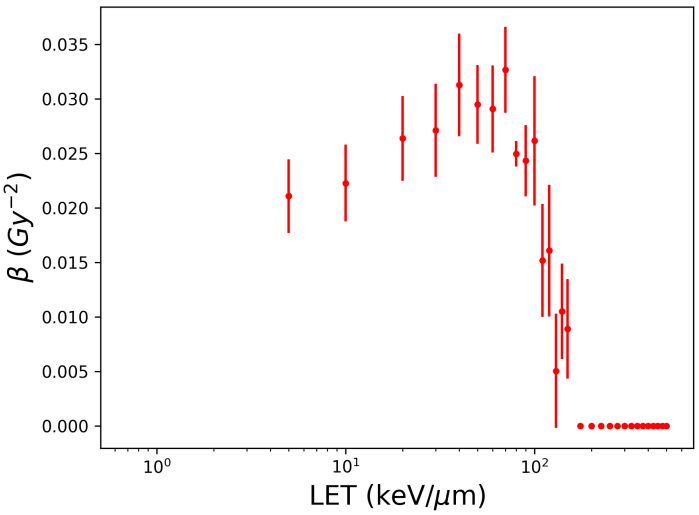

(f) β values for ions with $4 \leq Z \leq 8$

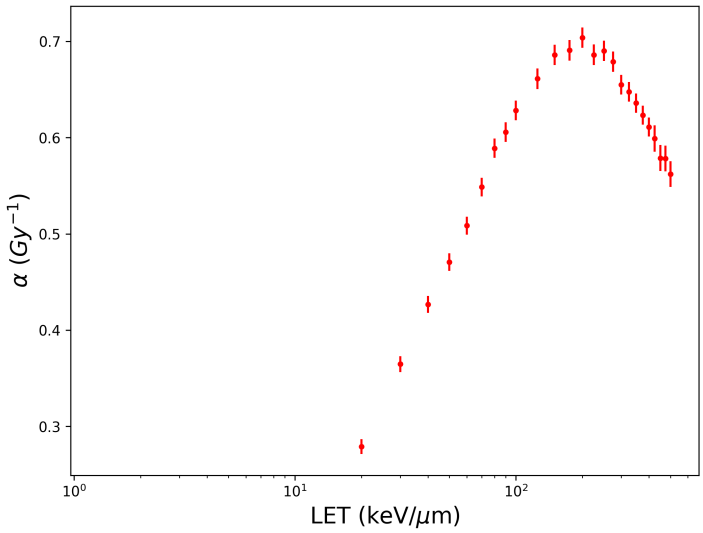

(g) α values for ions with $9 \leq Z \leq 14$

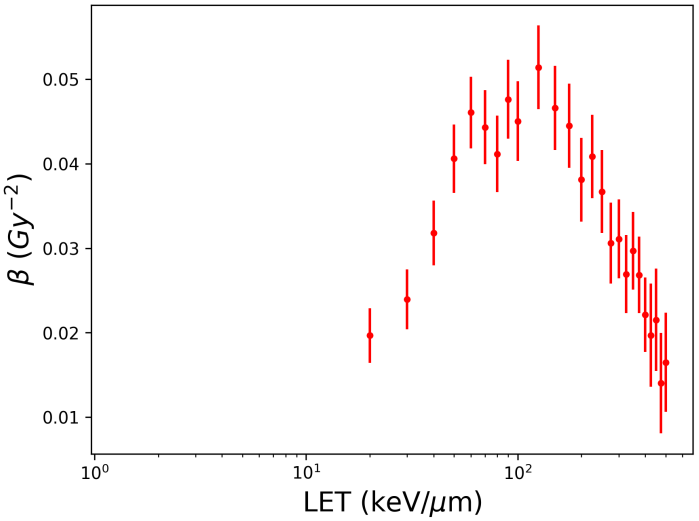

(h) β values for ions with $9 \leq Z \leq 14$

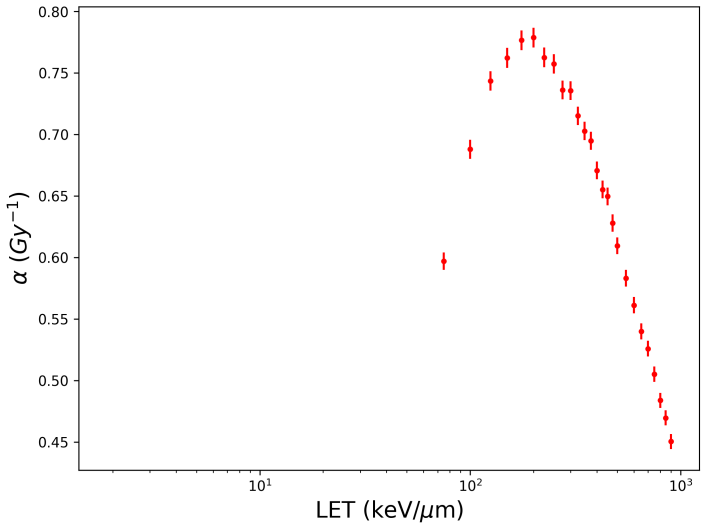

(i) α values for ions with $Z \geq 15$

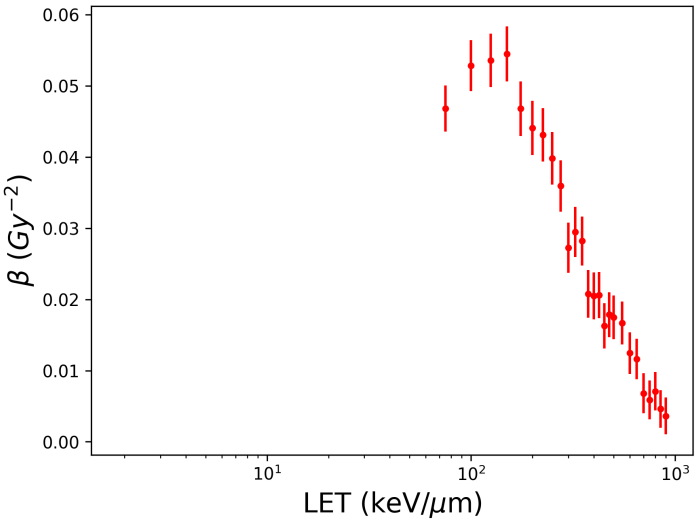

(j) β values for ions with $Z \geq 15$

Figure 3.6: α and β values for HaCaT and MCF10A for ions with $4 \leq Z \leq 8$, $9 \leq Z \leq 14$, and $Z \geq 15$ at various LET.

3.1.4 Comparison of the generated radiobiological databases

An interesting analysis is to compare the α and β values of HaCaT and MCF10A with those of Human Skin Fibloblast cell line to evaluate the radiosensitivity of different cell lines. For HSF, the BIANCA simulations were re-performed, and the values of the α and β parameters for the ions as a function of LET are plotted in Fig. 3.7 with green points while red points represent HaCaT and MCF10A. As with the HaCaT-MCF10A database, the associated uncertainties are derived from the LQ model fit, with the exception of neon and iron ions, for which the original database was used (since no corrections were performed) and no information regarding the errors is available.

Both the α and β values of HSF are always larger than those of HaCaT and MCF10A, which means that both the linear and quadratic components are more effective in producing damage; thus, for the same dose, the survival fraction of HSF is lower compared to HaCaT and MCF10A. This indicates that HSF cells are more radiosensitive than HaCaT and MCF10A cells.

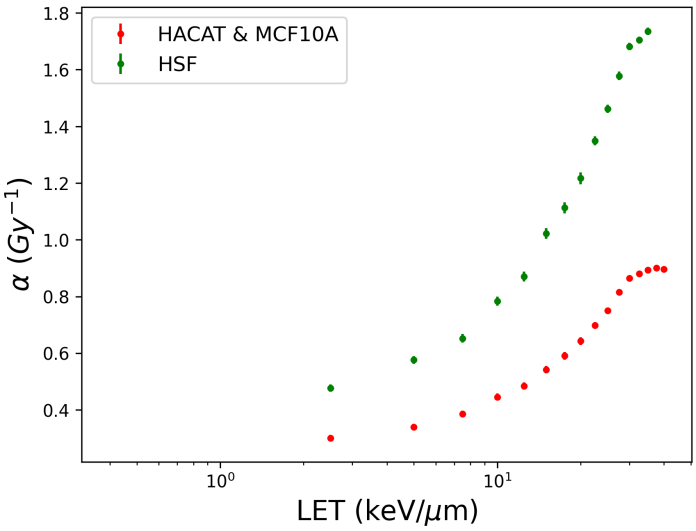

(a) α values for ions with $Z = 1$

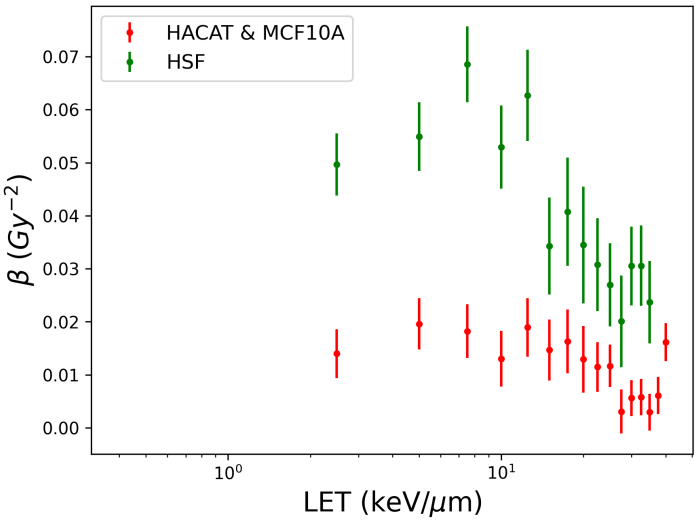

(b) β values for ions with $Z = 1$

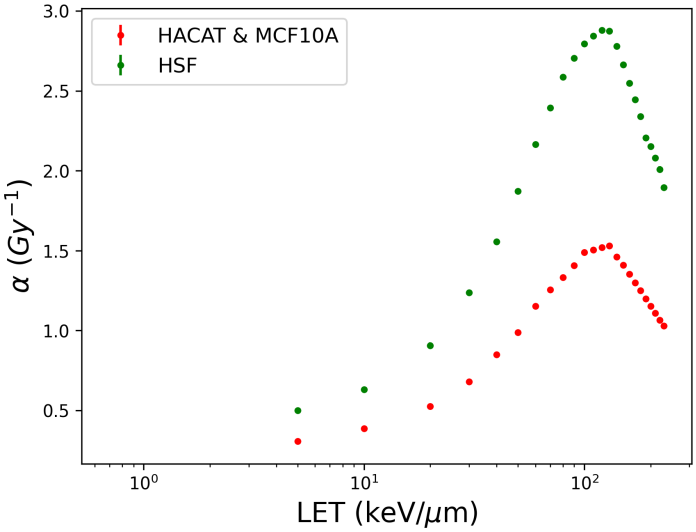

(c) α values for ions with $Z = 2$–3

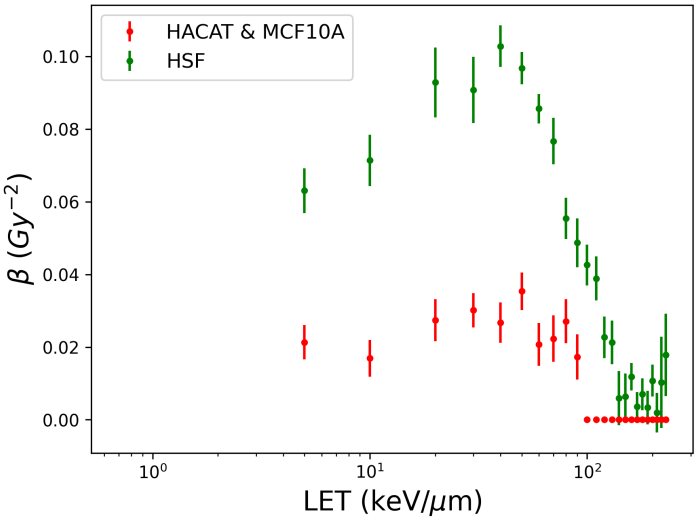

(d) β values for ions with $Z = 2$–3

Figure 3.7: Comparison of the α and β parameters as a function of LET for the HSF and the HaCaT and MCF10A radiobiological databases.

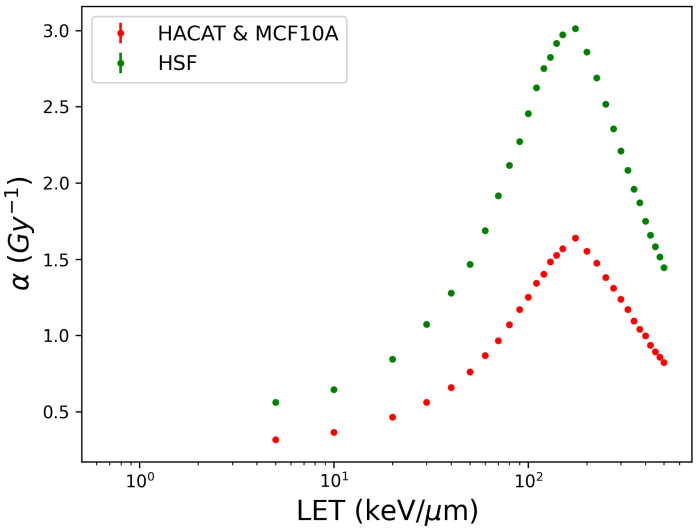

(e) α values for ions with $4 \leq Z \leq 8$

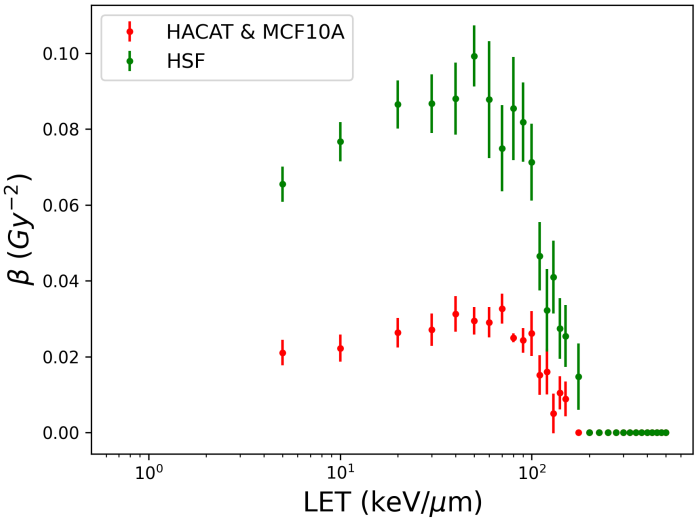

(f) β values for ions with $4 \leq Z \leq 8$

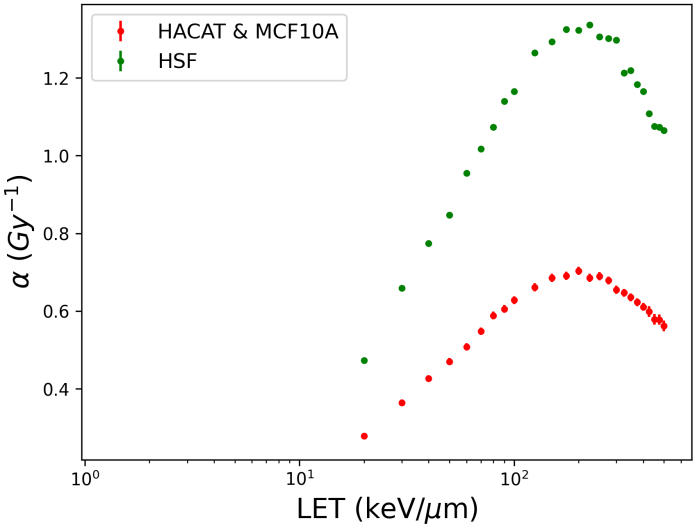

(g) α values for ions with $9 \leq Z \leq 14$

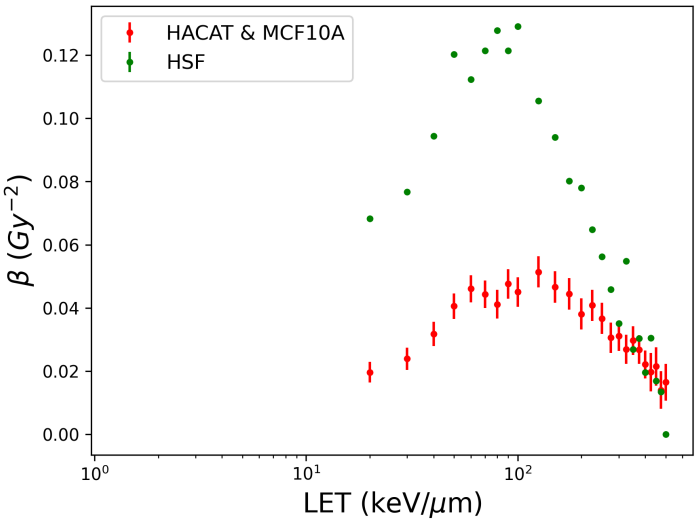

(h) β values for ions with $9 \leq Z \leq 14$

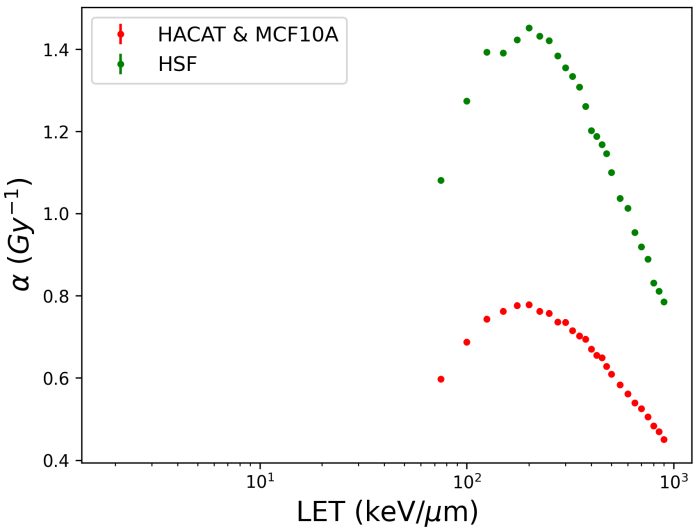

(i) α values for ions with $Z \geq 15$

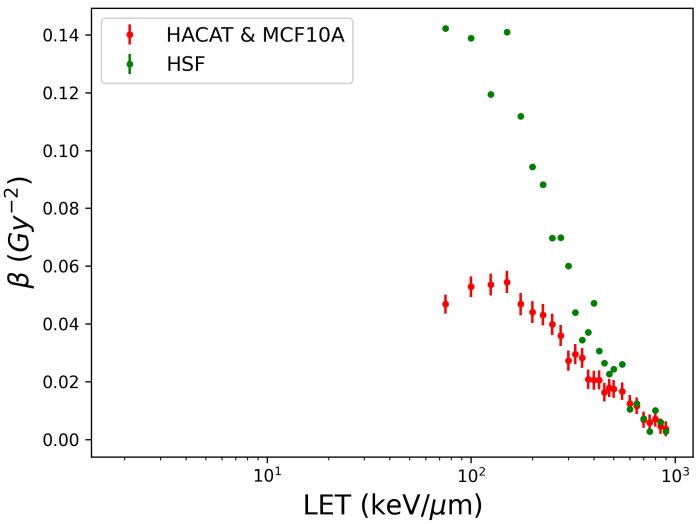

(j) β values for ions with $Z \geq 15$

Figure 3.7: Comparison of the α and β parameters as a function of LET for the HSF and the HaCaT and MCF10A radiobiological databases.

The generated cell-specific radiobiological databases constitute the basis for the calculation of the RBE-weighted absorbed dose presented in the following section. Since the HSF cell line exhibits a higher intrinsic radiosensitivity than the HaCaT and MCF10A cell lines for both photon and ion irradiation, differences in the predicted RBE-weighted absorbed dose are expected. The following chapter investigates how these differences translate into tissue-specific RBE-weighted dose distributions under the mixed radiation fields generated by the August 1972 Solar Particle Event.

3.2 Astronaut radiation exposure

This section presents the FLUKA simulations performed to evaluate the absorbed dose and the RBE-weighted absorbed dose in the skin of male and female phantoms, as well as in the female breast.

The calculations were carried out under different shielding conditions using the cell-specific radiobiological databases generated in the previous section. Finally, the influence of the Lea-Catcheside factor was investigated.

3.2.1 Absorbed dose

Before evaluating the differences in radiation response between fibroblasts and the HaCaT and MCF10A cell lines in the two organs of interest, namely the skin and the breast, following exposure to the August 1972 Solar Particle Event, it was first necessary to analyze the absorbed dose.

As described in Section 1.2, the absorbed dose is a purely physical quantity that represents the energy deposited by radiation per unit mass. Since it is independent of the cell line and biological response, it provides the baseline for the subsequent radiobiological analysis.

To evaluate the absorbed dose, both the male and female computational phantoms were placed inside aluminum shields with cylindrical and spherical shape. The shielding thickness was varied from 0.3 g/cm^2 to 35 g/cm^2[1]. The minimum value represented the shielding provided by a spacesuit during extravehicular activities (EVAs), whereas the maximum value represented a heavily shielded area inside the spacecraft designed to protect astronauts during solar particle events.

The absorbed doses for the skin in both male and female phantoms are plotted as a function of shielding thickness for the two different shield shapes in Fig. 3.8a

[1]Thickness is expressed as areal density (g/cm^2), calculated as the product of the geometric thickness (cm) and the material density (g/cm^3).

and Fig. 3.8b.

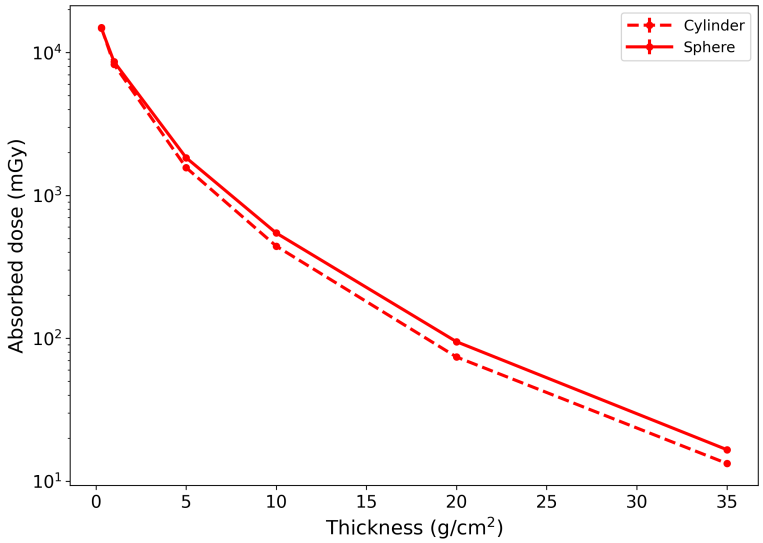

(a) Male phantom

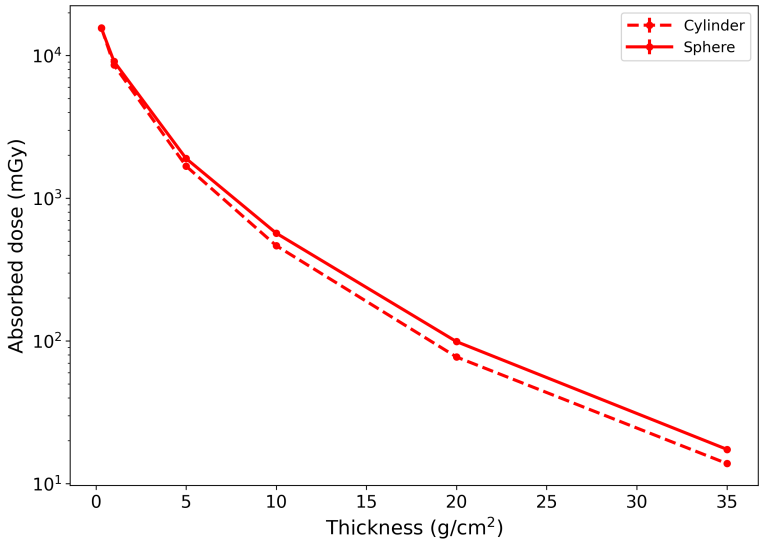

(b) Female phantom

Figure 3.8: Comparison of the absorbed dose to the skin for the male and female phantoms under cylindrical and spherical shielding configurations

Regarding the breast, the radiation effects were investigated using the female phantom. Female astronauts are playing an increasingly important role in modern space exploration, as exemplified by the Artemis II lunar mission, which includes a female Mission Specialist. Consequently, it is important to investigate radiation damage in female astronauts, with particular emphasis on female-specific organs such as the breast.

The absorbed dose to the female breast for the cylindrical and spherical shield-

ing configurations is shown in Fig. 3.9.

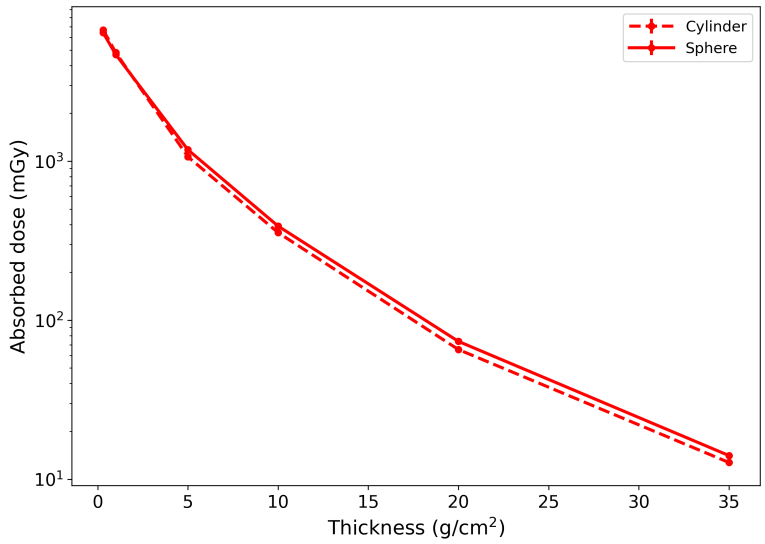

Figure 3.9: Comparison of the absorbed dose to the breast for the female phantom under cylindrical and spherical shielding configurations

The uncertainty associated with the absorbed dose is determined as described in Section 2.3.7 and is consistently less than 2% for both the skin and the breast. Due to their small magnitude relative to the plot symbols, the corresponding error bars are not visible.

As expected, the absorbed dose in both the skin and the breast decreases as the shielding thickness increases, regardless of the shielding geometry. This reduction is considerably more pronounced for the skin than for the breast, and a similar behavior would be expected for other internal organs. This effect can be explained by body self-shielding: internal organs are protected by the overlying tissues, which attenuate the radiation field before it reaches them. In contrast, the skin lacks this natural shielding and is directly exposed to the radiation transmitted through the external shield. Consequently, increasing the shielding thickness produces a larger relative reduction in absorbed dose for the skin than for internal organs.

In all three cases (Figs. 3.8a, 3.8b, and 3.9), the absorbed dose obtained with the spherical shielding is higher than that obtained with the cylindrical geometry. The only exception occurs at a shielding thickness of 0.3 g/cm^2, where the absorbed doses for both geometries are comparable within the statistical uncertainties. Nevertheless, the overall trend indicates higher absorbed doses for the spherical shield, with the relative difference peaking at 20% for female skin. This behavior can be explained by the fact that, in order to completely

enclose the phantom, the spherical shield must be larger than the cylindrical one (Fig. 3.8). Consequently, it intercepts a larger number of primary particles. In addition, for the same areal density, the spherical shield contains a larger total mass of aluminum, resulting in increased production of secondary particles and, consequently, a higher absorbed dose.

Another comparison can be made between the absorbed doses in the male and female phantoms for the same shielding geometry. The absorbed doses to the skin for the male and female phantoms as a function of shielding thickness are reported in Table 3.1a for the cylindrical geometry and in Table 3.1b for the spherical geometry.

Thickness (g/cm^2)	Absorbed dose (mGy)	
	Male	Female
0.3	14930	15650
1	8260	8590
5	1564	1678
10	442	465
20	73.9	77.2
35	13.29	13.84

(a) Cylindrical shield

Thickness (g/cm^2)	Absorbed dose (mGy)	
	Male	Female
0.3	14800	15560
1	8630	9100
5	1835	1898
10	545	569
20	94.5	98.9
35	16.58	17.39

(b) Spherical shield

Table 3.1: Comparison of the absorbed dose to the skin between the male and female phantoms under cylindrical and spherical shielding configurations.[2]

As shown in Tables 3.1a and 3.1b, the absorbed dose to the skin is consistently higher in the female phantom than in the male phantom for all shielding thicknesses and for both cylindrical and spherical geometries. This difference can be explained by the anatomical and geometrical characteristics of the two phantoms, as the female phantom is smaller and less massive than the male one.

[2]The statistical uncertainty associated with the absorbed dose values is less than 1% for each configuration. The number of significant digits reported is determined by the corresponding absolute uncertainty.

Consequently, body self-shielding is more effective in the male phantom. For example, when particles enter through the back of the body, they must traverse the torso before reaching the skin on the chest. Since the male phantom has a thicker torso, the radiation undergoes greater attenuation, resulting in fewer particles reaching the anterior skin than in the female phantom.

This finding is consistent with previous studies comparing radiation doses in male and female computational phantoms [47].

3.2.2 RBE-weighted Absorbed Dose

In this section, the impact of using the fibroblast database and the newly generated HaCaT and MCF10A database was evaluated. The quantity used for this comparison was the RBE-weighted absorbed dose, defined as the product of the absorbed dose and the RBE (Eq. 1.15) and expressed in units of mGy-Eq. The RBE-weighted absorbed dose was calculated using both radiobiological databases.

Figure 3.10 shows the RBE-weighted absorbed dose to the skin of the male phantom for the cylindrical and spherical shielding geometries, while Figure 3.11 presents the corresponding results for the female phantom. In both figures, the horizontal black line represents the NASA 30-day limit for tissue reactions in the skin (1.5 Gy-Eq), see Table 1.3). According to this limit, an aluminum shielding thickness of approximately 10 g/cm^2 is required to maintain the RBE-weighted absorbed dose below the recommended value.

A similar analysis was performed for the female breast, and the corresponding results are shown in Figure 3.12. The RBE-weighted absorbed dose was calculated using both the fibroblast and the HaCaT and MCF10A databases. Unlike the skin, however, NASA has not established specific dose limits for tissue reactions in the breast.

The uncertainty associated with the RBE-weighted absorbed dose is calculated from the 5 independent runs performed for each configuration, following the methodology described in Section 2.3.7.

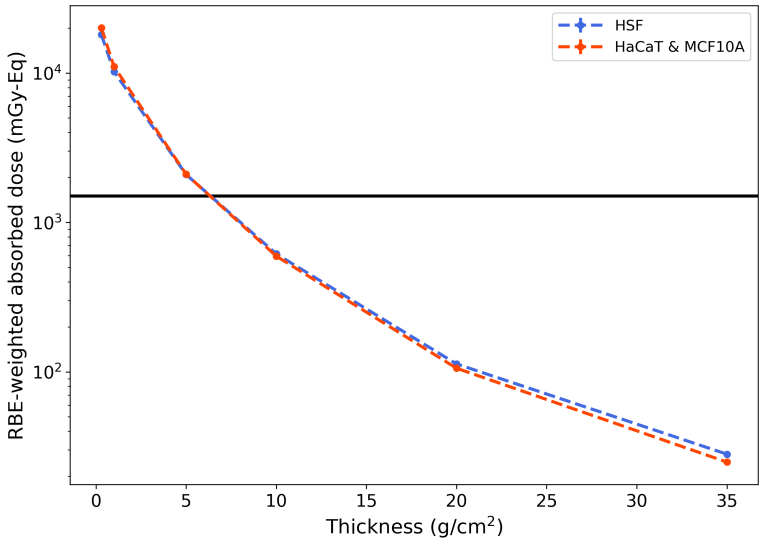

(a) Cylinder

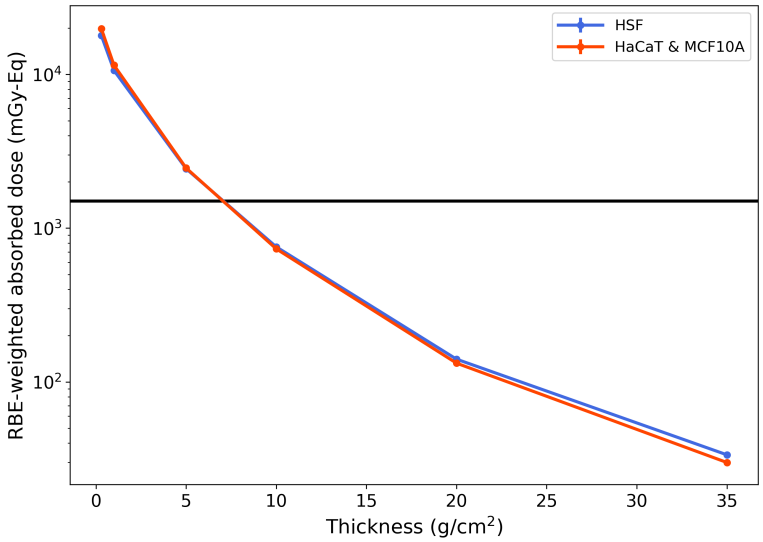

(b) Sphere

Figure 3.10: Comparison of RBE weighted absorbed dose to the skin within cylindrical and spherical shield for male phantom

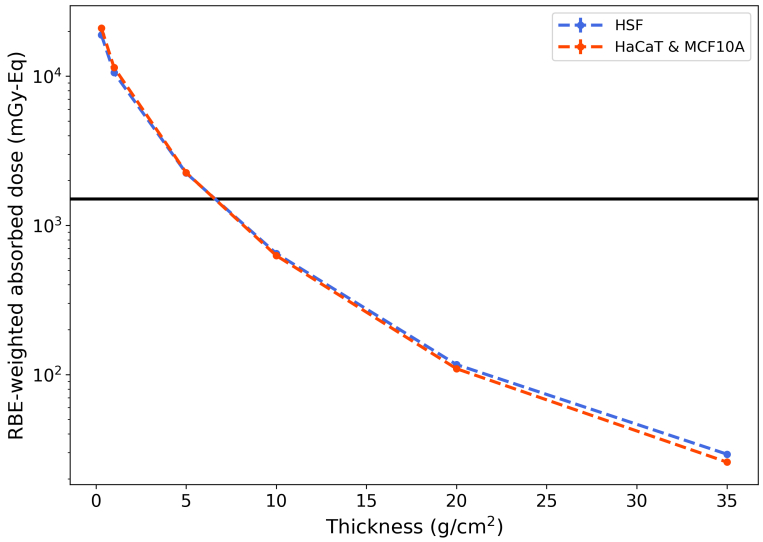

(a) Cylinder

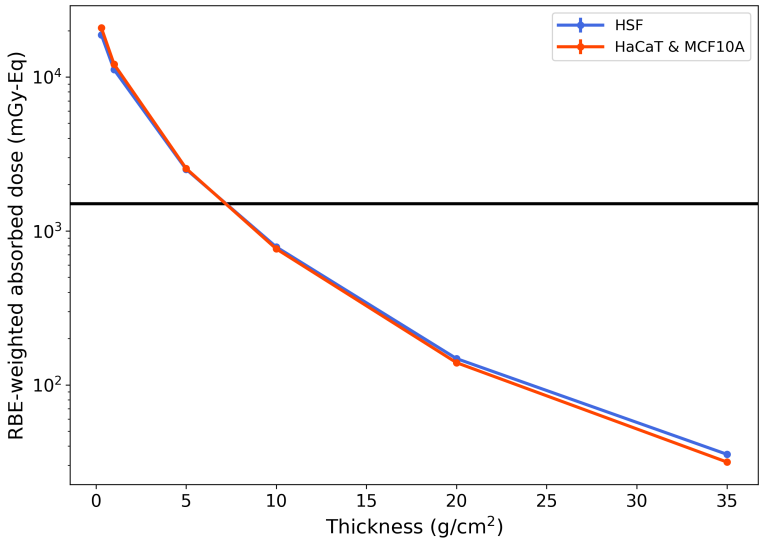

(b) Sphere

Figure 3.11: Comparison of RBE weighted abosrbed dose to the skin within cylindrical and spherical shield for female phantom

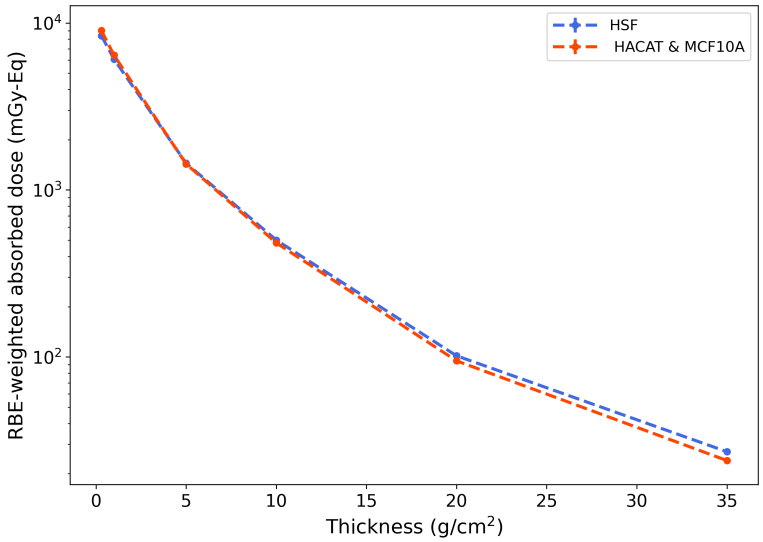

(a) Cylinder

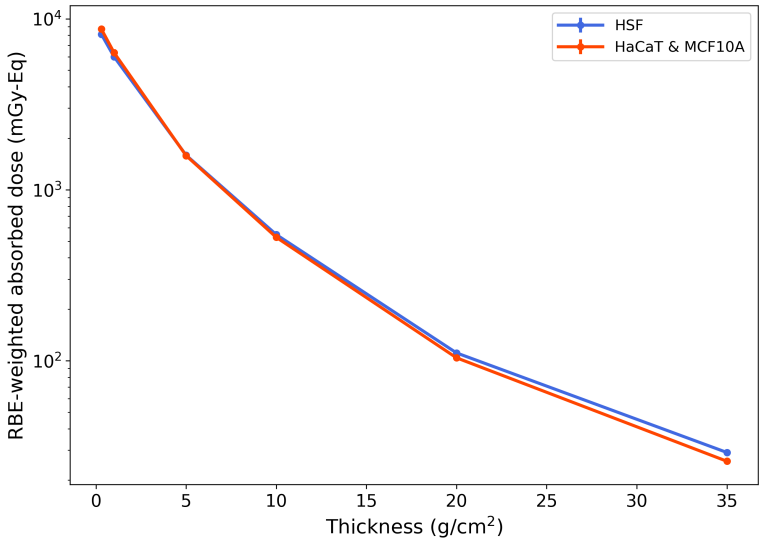

(b) Sphere

Figure 3.12: Comparison of RBE weighted absorbed dose to the breast within cylindrical and spherical shield for female phantom

Concerning the comparison between the fibroblast and the HaCaT and MCF10A databases, the observed trend is not straightforward. As shown in Figs. 3.10, 3.11, and 3.12, the RBE-weighted absorbed dose calculated using the HaCaT and MCF10A database is higher up to a shielding thickness between approximately 5 and 10 g/cm^2. Beyond this threshold, the fibroblast database yields higher RBE-weighted absorbed dose values.

To better quantify this behavior, the relative difference between the two databases was calculated as:

$$\text{Rel. Diff.} = \frac{(\text{RBE-D}_{\text{HSF}}) - (\text{RBE-D}_{\text{HaCaT/MCF10A}})}{\text{RBE-D}_{\text{HSF}}} \tag{3.1}$$

where RBE-D denotes the RBE-weighted absorbed dose.

The relative differences between the two databases are shown in Figs. 3.13a and 3.13b for the skin of the male phantom, in Figs. 3.14a and 3.14b for the skin of the female phantom, and in Figs. 3.15a and 3.15b for the female breast, considering both cylindrical and spherical shielding geometries. The uncertainty in the relative difference is determined from the RBE-weighted absorbed dose values and their corresponding errors through the application of error propagation.

For all shielding geometries, organs, and phantoms, the relative difference is initially negative up to approximately 5 g/cm^2, after which it becomes positive. This indicates that, for low shielding thicknesses, the RBE-weighted absorbed dose calculated using the HaCaT and MCF10A database is higher than that obtained using the fibroblast database, whereas the opposite behavior is observed for larger shielding thicknesses. This behavior can be explained by the combined effect of the LET-dependent radiobiological parameters and the nonlinear formulation of the RBE calculation. Although the HSF cell line exhibits higher intrinsic radiosensitivity, reflected by larger α and β values, the RBE depends on both the photon reference parameters and their evolution with LET. As the shielding thickness increases, the particle energy spectrum and the corresponding LET distribution inside the phantom change because of the attenuation of primary particles and the production of secondary radiation. Consequently, different regions of the radiobiological databases become relevant to the calculation, leading to a change in the relative RBE-weighted absorbed dose predicted by the two databases.

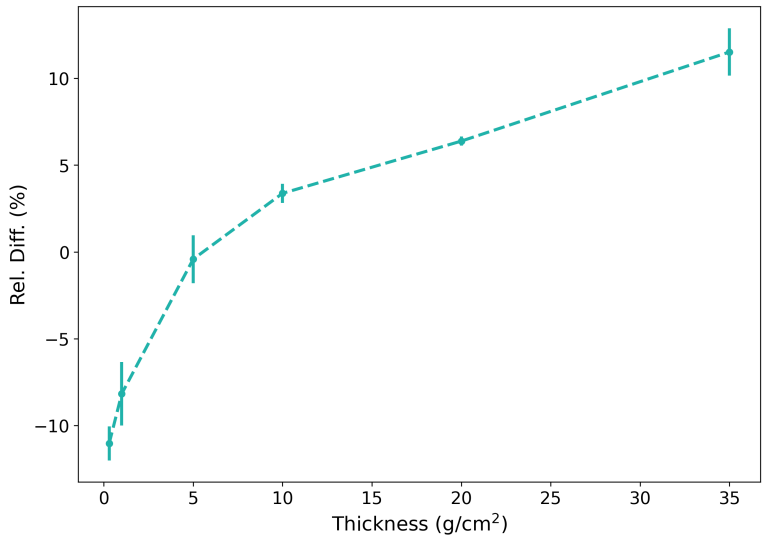

(a) Cylinder

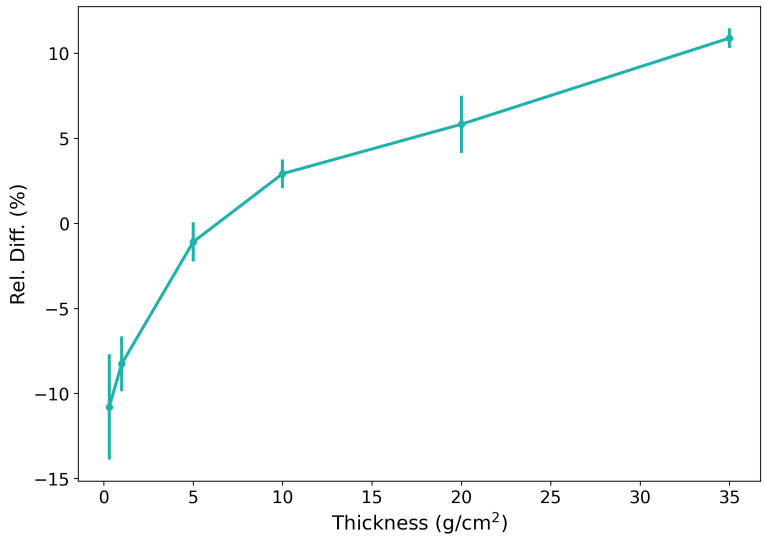

(b) Sphere

Figure 3.13: Relative difference between RBE-weighted absorbed dose with fibroblast and HaCaT and MCF10A database in skin for male phantom with cylindrical and spherical shielding

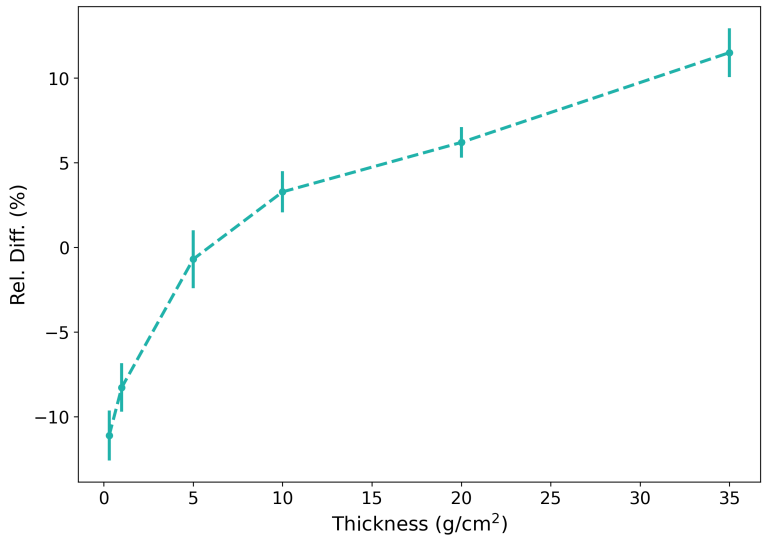

(a) Cylinder

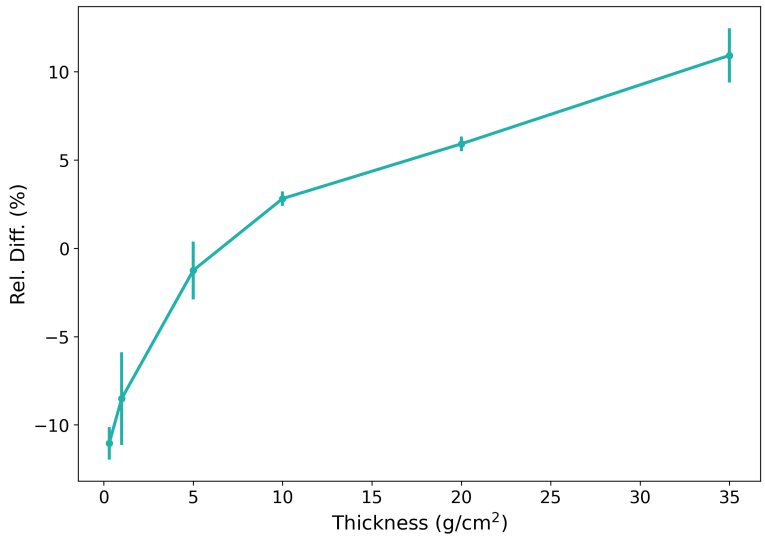

(b) Sphere

Figure 3.14: Relative difference between RBE-weighted absorbed dose with fibroblast and HaCaT and MCF10A database in skin for female phantom with cylindrical and spherical shielding

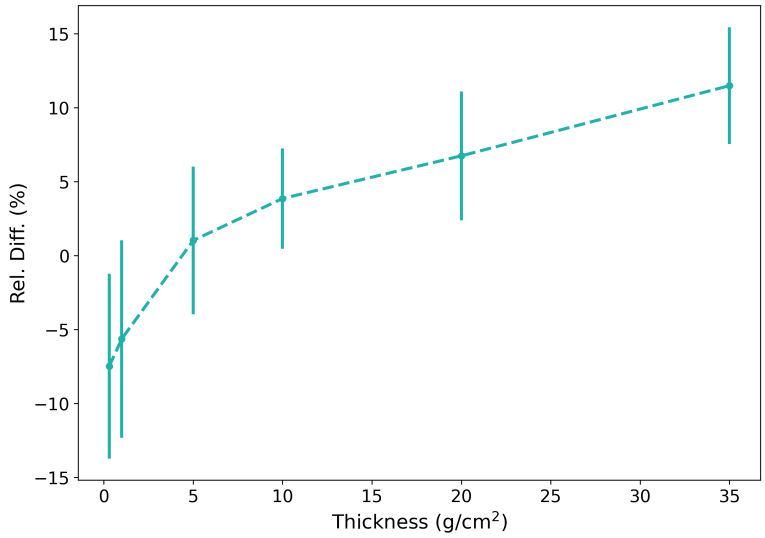

(a) Cylinder

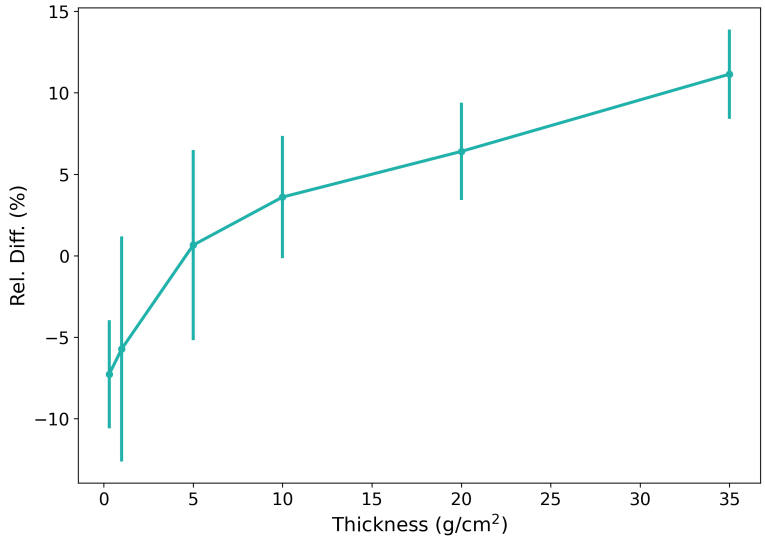

(b) Sphere

Figure 3.15: Relative difference between RBE-weighted absorbed dose with fibroblast and HaCaT and MCF10A database in breast for female phantom with cylindrical and spherical shielding

Overall, the results demonstrate that the choice of the radiobiological database has a significant impact on the predicted RBE-weighted absorbed dose. In particular, the HaCaT-MCF10A database provides more conservative estimates for low shielding thicknesses (approximately below 5–10 g/cm^2), whereas the fibroblast database becomes more conservative for larger shielding thicknesses. These findings highlight the importance of using cell-specific radiobiological databases when assessing radiation risk in space environments, since the predicted biological response may vary considerably depending on the tissue considered.

It should be noted that all the results presented in this section were obtained assuming an instantaneous irradiation. However, unlike particle therapy, Solar Particle Events extend over several hours, allowing sublethal DNA damage repair to occur during irradiation. Consequently, the biological effectiveness of the delivered dose may be reduced. To account for this temporal effect, the influence of the Lea-Catcheside factor is investigated in the following section.

3.3 Temporal effects and sublethal damage repair

Unlike the calculations presented in the previous section, the radiation dose delivered during the August 1972 Solar Particle Event was not received instantaneously but was spread over several hours. As a result, cells had sufficient time to repair part of the sublethal DNA damage while irradiation was still ongoing. This phenomenon can be accounted for through the Lea-Catcheside factor, as described in Section 2.1.2.

The aim of this section was to quantify the impact of dose protraction and sublethal damage repair on the predicted RBE-weighted absorbed dose.

The parameters required for the calculation of the Lea-Catcheside factor, namely the half-times of the fast and slow repair components and their corresponding partition coefficients, were taken from [19].

Since repair kinetics for the HaCaT and MCF10A cell lines have not yet been reported in the literature, the repair parameters determined for HSF cells were also used for these cell lines. According to [19], for high-LET radiation the fast repair component is characterized by a half-time of $T_{1/2} = 25$ min, whereas the slow repair component has a half-time of $T_{1/2} = 78$ min, with partition coefficients of 35% and 65%, respectively.

The influence of the Lea-Catcheside factor on the RBE-weighted absorbed dose was evaluated using both the HSF and the HaCaT and MCF10A radiobiological databases.

The analysis is performed for the worst-case scenario, namely the one in which the highest dose is received. For the skin, this corresponds to the female phantom inside the spherical shield; the same configuration is applied to the evaluation of the breast.

Four different irradiation times are considered: 2 h, 4 h, 16 h, and the case of acute irradiation already studied. In the latter, the exposure time is taken as zero, meaning the Lea-Catcheside factor reduces to 1.

The RBE-weighted absorbed doses in the skin as a function of shielding thickness for the various irradiation times are presented in Fig. 3.16a for the HaCaT-MCF10A database and in Fig. 3.16b for the HSF database where the horizontal line represent 30 day NASA limit for tissue reactions. Similarly, the corresponding results for the breast are shown in Figs. 3.17a and 3.17b. Analogously to the RBE-weighted absorbed dose, the associated uncertainty is evaluated following the methodology detailed in Section 2.3.7, under the assumption that the Lea-Catcheside factor carries no intrinsic uncertainty.

To further analyze the impact of exposure protraction, the relative differences between acute irradiation and the $T = 16$ h case (corresponding to the duration of the August 1972 SPE) are illustrated in Fig. 3.18a for the skin and Fig. 3.18b for the breast. The error associated with the relative difference is calculated via error propagation from the RBE-weighted absorbed dose values and their respective uncertainties.

For both organs and cell lines, it is evident that the relative difference between acute and protracted irradiation diminishes as shielding thickness increases. For instance, for the skin using the HSF database, the difference is around 35% at 0.3 g/cm^2, dropping to 5% at 10 g/cm^2. This occurs because greater shielding thicknesses reduce particle energy, leading to a higher LET compared to thinner configurations. At high LET, the linear parameter α of the LQ model is predominant over β, meaning that the modulation introduced by the Lea-Catcheside factor G (which scales the quadratic term) has a smaller overall impact.

Furthermore, as illustrated in both panels of Fig. 3.18, the relative difference between acute and protracted scenarios is consistently higher for the HSF database than for the HaCaT-MCF10A database. This behavior is explained by the fact that the HSF database exhibits a higher β parameter; consequently, the application of factor G induces a more pronounced variation in the biological effect.

Comparing the two graphs in Fig. 3.18, it is observable that the relative difference between acute and protracted irradiation in the skin is higher compared

to that in the breast. The reason is analogous to the one provided for the decrease observed with increasing shielding thickness. In fact, since the breast is an internal organ while the skin is a superficial one, the breast benefits from a higher self-shielding effect.

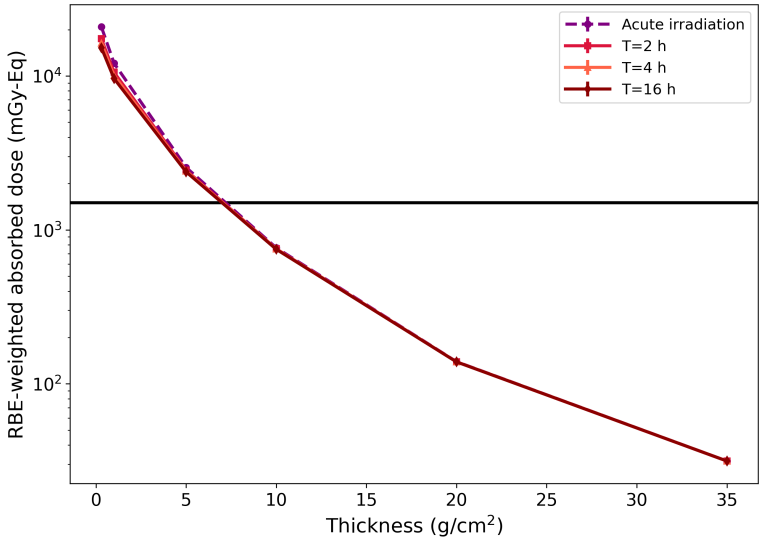

(a) HaCaT-MCF10A

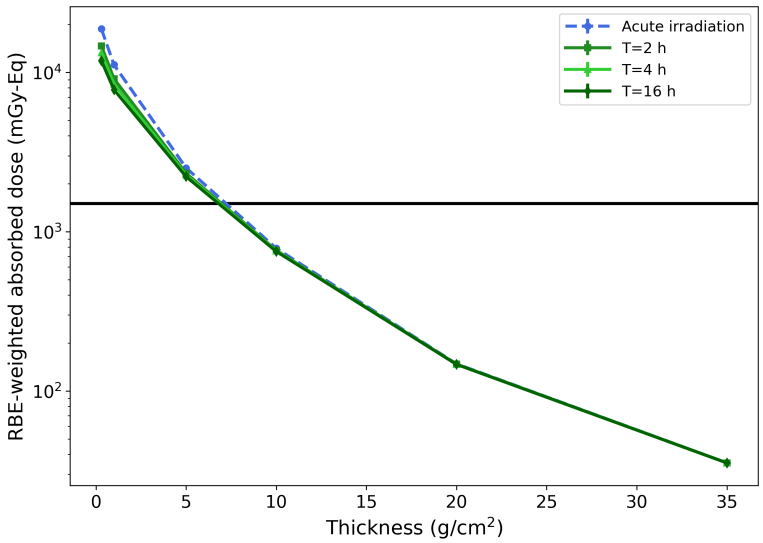

(b) HSF

Figure 3.16: Comparison of RBE weighted absorbed dose to the skin at different irradiation time in female phantom within spherical shielding

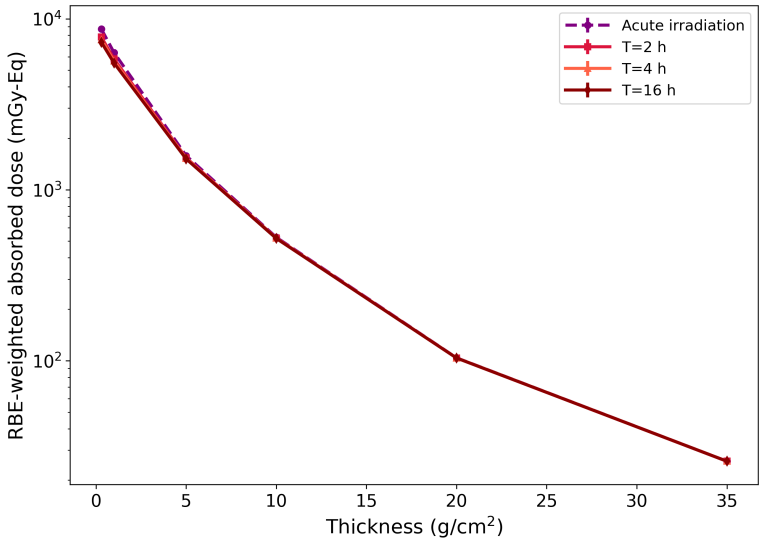

(a) HaCaT-MCF10A

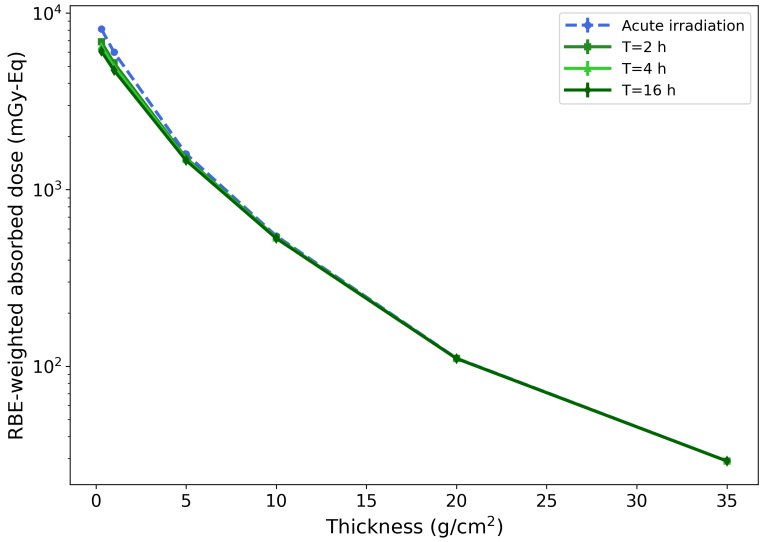

(b) HSF

Figure 3.17: Comparison of RBE weighted absorbed dose to the breast at different irradiation time in female phantom within spherical shielding

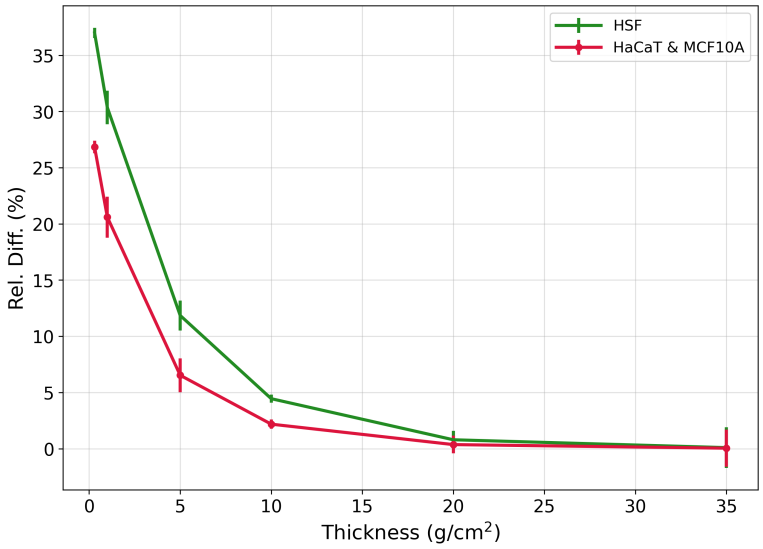

(a) Skin

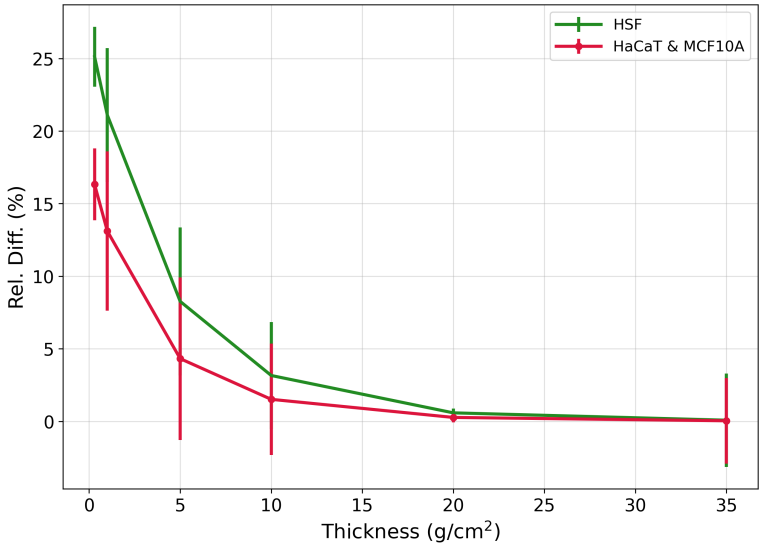

(b) Breast

Figure 3.18: Relative difference between RBE-weighted absorbed dose with acute irradiation or irradiation time of 16 h in skin and breast of female phantom within spherical shielding

These findings underline the importance of considering radiation exposure as a protracted event over time, since the values can vary by up to 35% in the most extreme case. Nonetheless, quantifying the RBE-weighted dose assuming an acute irradiation scenario remains conservative from a radiation protection perspective, as acute exposure consistently yields higher RBE-weighted absorbed doses.

CHAPTER 4

Conclusions

This work focused on the generation of cell-specific radiobiological databases for the HaCaT and MCF10A cell lines using the BIANCA model. These cell lines were selected because they represent two tissues of particular relevance for space radiation protection. HaCaT cells are immortalized human keratinocytes and therefore represent the skin, which is one of the organs most exposed during Solar Particle Events due to its superficial location. MCF10A cells are non-tumorigenic human mammary epithelial cells and were selected to represent breast tissue, whose radiobiological response is becoming increasingly important owing to the growing participation of women in human space exploration.

The first objective of this work was to generate and validate these new radiobiological databases. The photon response of the HaCaT and MCF10A cell lines was first characterized, allowing the determination of the BIANCA model parameters CL and f. Subsequently, the model was successfully validated against the available experimental data for proton and carbon ion irradiations, demonstrating that the predicted survival curves accurately reproduced the experimental observations. Once validated, the model was used to generate LET-dependent α and β parameters for the ion species relevant to the space radiation environment. This is the first application of the BIANCA model to generate radiobiological databases for the HaCaT and MCF10A cell lines for space radiation applications.

Comparison of the generated databases with the updated Human Skin Fibroblast (HSF) database showed that fibroblasts exhibit consistently higher α and β values over the investigated LET range, indicating a greater intrinsic ra-

diosensitivity than the HaCaT and MCF10A cell lines. These results highlight the importance of developing tissue-specific radiobiological databases rather than relying on a single reference cell line when evaluating the biological effects of space radiation.

The generated databases were subsequently coupled with FLUKA Monte Carlo simulations to investigate radiation exposure during the August 1972 Solar Particle Event. The absorbed dose analysis showed that increasing the shielding thickness substantially reduced the dose delivered to both the skin and the breast. The reduction was more pronounced for the skin because internal organs benefit from body self-shielding. In addition, spherical shielding geometries systematically produced higher absorbed doses than cylindrical geometries owing to their larger dimensions and the resulting increase in secondary particle production.

The choice of radiobiological database was found to significantly influence the predicted RBE-weighted dose. Specifically, it displayed an inversion dependent on the shielding thickness, with the HaCaT-MCF10A database yielding higher values below a certain threshold and the HSF database becoming dominant at larger thicknesses. At the minimum shielding thickness evaluated (0.3 g/cm^2), the RBE-weighted dose obtained with the HaCaT-MCF10A database was approximately 10% higher than that of the HSF database, whereas at the maximum thickness (35 g/cm^2), the trend reversed and the HSF database provided values over 10% higher than the new database. These findings demonstrate that the predicted biological response depends not only on the intrinsic radiosensitivity of the selected cell line, but also on the LET dependence of the radiobiological parameters and on the characteristics of the mixed radiation field.

Finally, the temporal profile of the August 1972 Solar Particle Event was incorporated through the application of the Lea-Catcheside factor. By accounting for sublethal DNA damage repair during the several hours of irradiation, lower RBE-weighted absorbed doses were obtained than those predicted assuming instantaneous dose delivery. This effect was particularly significant at low shielding thicknesses, for the HSF cell line and for superficial organs such as the skin. In this specific configuration, the relative difference between acute exposure and a 16-hour protracted irradiation reached 35%. These findings highlight the importance of considering dose protraction and DNA repair processes when assessing the biological consequences of Solar Particle Events.

Overall, this work demonstrates that the integration of Monte Carlo particle transport simulations with cell-specific radiobiological modeling provides a powerful tool for the evaluation of space radiation effects. The radiobiological

databases generated in this work can be directly coupled with particle transport calculations to estimate tissue-specific biological effectiveness, thereby improving the assessment of astronaut radiation exposure during Solar Particle Events.

Appendix

	a (Gy/cell)	b $(\text{keV}/\mu\text{m})^{-1}$	c $(\text{keV}/\mu\text{m})^{-2}$	d $(\text{keV}/\mu\text{m})^{-1}$
Protons	10.2101	1.71E-06	8.87E-09	2.06E+07
He	0.00239286	0.00452309	0.000105849	1.28E+11
C	0.00728628	0.00276319	2.62E-05	699525
Ne	0.0695119	0.0040857	0	0.0924697
Fe	0.179083	0.0109239	0	0.00591672

Table 1: Fit parameters for the $CL(LET)$ equation (Eq. 2.10) for V79 cells where CL is expressed in $\text{CL}\,\text{Gy}^{-1}\,\text{cell}^{-1}$ and LET in $\text{keV}/\mu\text{m}$. Parameters a, b, c and d are reported for different particle types.

	a	c	X
Protons	0.05429	0.44	30
He	0.07194	0.60	131
C	0.0733	0.65	172

Table 2: Fit parameters for $f(LET)$ as defined in Eq. 2.11 for V79 cells; f has no unit of measure and LET is expressed in $\text{keV}/\mu\text{m}$. For Ne and Fe, f is constant and equal at 0.8

Bibliography

[1] NASA. *Human System Risks*. https://www.nasa.gov/hhp/human-system-risks/. 2024.

[2] M. S. Clowdsley, J. E. Nealy, W. Atwell, B. M. Anderson, N. A. Luetke, and J. W. Wilson. *Calculation of Radiation Protection Quantities and Analysis of Astronaut Orientation Dependence*. NASA Technical Paper NASA/TP-2006-214296. National Aeronautics and Space Administration, 2006.

[3] Z. S. Patel, T. J. Brunstetter, W. J. Tarver, A. M. Whitmire, S. R. Zwart, S. M. Smith, and J. L. Huff. "Red risks for a journey to the red planet: The highest priority human health risks for a mission to Mars". In: *npj Microgravity* 6.1 (2020), p. 22. DOI: 10.1038/s41526-020-00124-6.

[4] L. W. Townsend. "Implications of the space radiation environment for human exploration in deep space". In: *Radiat. Prot. Dosimetry* 115.1–4 (2005), pp. 44–50. DOI: 10.1093/rpd/nci133.

[5] M. Durante and F. A. Cucinotta. "Physical basis of radiation protection in space travel". In: *Rev. Mod. Phys.* 83.4 (2011), pp. 1245–1281. DOI: 10.1103/RevModPhys.83.1245.

[6] G. A. Nelson. "Space Radiation and Human Exposures, A Primer". In: *Radiat. Res.* 185.4 (2016), pp. 349–358. DOI: 10.1667/RR14311.1.

[7] L. C. Simonsen, T. C. Slaba, P. Guida, and A. Rusek. "NASA's first ground-based Galactic Cosmic Ray Simulator: Enabling a new era in space radiobiology research". In: *PLOS Biol.* 18.5 (2020), e3000669. DOI: 10.1371/journal.pbio.3000669.

[8] S. Hu. *Solar Particle Events and Radiation Exposure in Space*. Tech. rep. NASA Johnson Space Center, 2017. URL: https://three.jsc.nasa.gov/articles/hu-spes.pdf.

[9] P. Jiggens, M.-A. Chavy-Macdonald, G. Santin, A. Menicucci, H. Evans, and A. Hilgers. "The magnitude and effects of extreme solar particle events". In: *J. Space Weather Space Clim.* 4 (2014), A20. DOI: 10.1051/swsc/2014017.

[10] D. J. Knipp, B. J. Fraser, M. A. Shea, and D. F. Smart. "On the Little-Known Consequences of the 4 August 1972 Ultra-Fast Coronal Mass Ejecta: Facts, Commentary, and Call to Action". In: *Space Weather* 16.11 (2018), pp. 1607–1610. DOI: 10.1029/2018SW002024.

[11] B. T. Tsurutani, A. Sen, R. Hajra, G. S. Lakhina, R. B. Horne, and T. Hada. "Review of the August 1972 and March 1989 (Allen) Space Weather Events: Can We Learn Anything New From Them?" In: *J. Geophys. Res. Space Phys.* 129.7 (2024), e2024JA032622. DOI: 10.1029/2024JA032622.

[12] International Commission on Radiological Protection. "Assessment of Radiation Exposure of Astronauts in Space". In: *Ann. ICRP (ICRP Publication 123)* 43.1 (2013), pp. 1–148. DOI: 10.1016/j.icrp.2013.05.004.

[13] W. R. Leo. *Techniques for Nuclear and Particle Physics Experiments: A How-to Approach*. 2nd. Berlin, Heidelberg: Springer-Verlag, 1994. DOI: 10.1007/978-3-642-57920-2.

[14] J. C. McPhee and J. B. Charles. *Human Health and Performance Risks of Space Exploration Missions: Evidence Reviewed by the NASA Human Research Program*. NASA Special Publication NASA SP-2009-3405. Houston, TX: National Aeronautics and Space Administration, 2009.

[15] National Aeronautics and Space Administration. *NASA Spaceflight Human-System Standard: Volume 1, Revision B: Crew Health*. NASA Standard NASA-STD-3001 VOL 1 REV B. NASA, 2022.

[16] F. A. Cucinotta. *Space Radiation Risk Acceptability and Limitations*. NASA Technical Report NASA/TM-2010-216122. NASA Johnson Space Center, 2010.

[17] T. Komiyama. "Practicalities of dose management for Japanese astronauts staying at the International Space Station". In: *Ann. ICRP* 49.1_suppl (2020), pp. 189–198. DOI: 10.1177/0146645320941328.

[18] S. J. McMahon. "The linear quadratic model: usage, interpretation and challenges". In: *Phys. Med. Biol.* 64.1 (2019), 01TR01. DOI: 10.1088/1361-6560/aaf26a.

[19] E. I. Canay et al. "Incorporation of dose-rate effects into the BIANCA biophysical model and application for space radiation risk assessment". In: *Life Sci. Space Res.* 44 (2025), pp. 72–81. DOI: 10.1016/j.lssr.2025.01.001.

[20] D. J. Brenner. "The Linear-Quadratic Model Is an Appropriate Methodology for Determining Isoeffective Doses at Large Doses Per Fraction". In: *Semin. Radiat. Oncol.* 18.4 (2008), pp. 234–239. DOI: 10.1016/j.semradonc.2008.04.004.

[21] W. T. Millar and J. W. Hopewell. "Effects of very low dose-rate ^{90}Sr/^{90}Y exposure on the acute moist desquamation response of pig skin". In: *Radiother. Oncol.* 84.2 (2007), pp. 209–215. DOI: 10.1016/j.radonc.2007.04.028.

[22] R. L. Ramos, A. Embriaco, M. P. Carante, A. Ferrari, P. Sala, V. Vercesi, and F. Ballarini. "Radiobiological damage by space radiation: extension of the BIANCA model to heavy ions up to iron, and pilot application to cosmic ray exposure". In: *J. Radiol. Prot.* 42.2 (2022), p. 021503. DOI: 10.1088/1361-6498/ac5d48.

[23] R. L. Ramos, A. Embriaco, M. P. Carante, A. Ferrari, P. Sala, V. Vercesi, and F. Ballarini. "Extension of the BIANCA biophysical model up to Fe-ions and applications for space radiation research". In: *EPJ Web Conf.* 261 (2022), p. 01004. DOI: 10.1051/epjconf/202226101004.

[24] M. P. Carante, C. Aimè, J. J. T. Cajiao, and F. Ballarini. "BIANCA, a biophysical model of cell survival and chromosome damage by protons, C-ions and He-ions at energies and doses used in hadrontherapy". In: *Biomed. Phys. Eng. Express* 4.6 (2018), p. 065008. DOI: 10.1088/2057-1976/aae43a.

[25] Coriell Institute for Medical Research. *Coriell Cell Catalog: AG01522*. https://catalog.coriell.org/0/Sections/Search/Sample_Detail.aspx?Ref=AG01522. 2024.

[26] Expasy Cellosaurus. *Cellosaurus entry CVCL_H759 (AG01522)*. https://www.cellosaurus.org/CVCL_H759. 2024.

[27] National Human Genome Research Institute. *Talking Glossary of Genomic and Genetic Terms: Fibroblast*. https://www.genome.gov/genetics-glossary/Fibroblast. 2024.

[28] R. Wong, S. Geyer, W. Welling, E. Bradbury, and T. H. Liyanage. "Anatomy, physiology and function of all skin layers and impact of ageing skin". In: *Wound Pract. Res.* 24.1 (2016), pp. 2–12.

[29] Cytion Cell Line Service. *HaCaT Cell Line Specification*. https://www.cytion.com/HaCaT-Cells/300493. 2024.

[30] P. Boukamp, R. T. Petrussevska, D. Breitkreutz, J. Hornung, A. Markham, and N. E. Fusenig. "Normal keratinization in a spontaneously immortalized aneuploid human keratinocyte cell line". In: *J. Cell Biol.* 106.3 (1988), pp. 761–771. DOI: 10.1083/jcb.106.3.761.

[31] H. Yousef, M. Alhajj, A. O. Fakoya, and S. Sharma. "Anatomy, Skin (Integument), Epidermis". In: *StatPearls*. Treasure Island (FL): StatPearls Publishing, 2024.

[32] Cleveland Clinic. *Epidermis Overview*. https://my.clevelandclinic.org/health/body/21901-epidermis. 2022.

[33] Cytion Cell Line Service. *MCF10A Cell Line Specification*. https://www.cytion.com/MCF10A-Cells/305026. 2024.

[34] A. Fassò, A. Ferrari, P. R. Sala, et al. *The FLUKA Code: Manual*. 2021.

[35] J. W. Wilson, F. F. Badavi, F. A. Cucinotta, J. L. Shinn, G. D. Badhwar, R. Silberberg, C. H. Tsao, L. W. Townsend, and R. K. Tripathi. *HZETRN: Description of a Free-Ion and Nucleon Transport and Shielding Computer Program*. NASA Technical Paper NASA-TP-3495. National Aeronautics and Space Administration, 1995.

[36] D. L. Bertsch, S. Biswas, and D. V. Reames. "Solar cosmic ray composition above 10 MeV/nucleon and its energy dependence in the 4 August 1972 event". In: *Sol. Phys.* 31.1 (1973), pp. 247–267. DOI: 10.1007/BF00732800.

[37] International Commission on Radiological Protection. "Basic Anatomical and Physiological Data for Use in Radiological Protection: Reference Values". In: *Ann. ICRP (ICRP Publication 89)* 32.3–4 (2002), pp. 1–277. DOI: 10.1016/S0146-6453(03)00002-2.

[38] International Commission on Radiological Protection. "Adult Reference Computational Phantoms". In: *Ann. ICRP (ICRP Publication 110)* 39.2 (2009), pp. 1–166. DOI: 10.1016/j.icrp.2009.09.001.

[39] E. Mara, M. Clausen, S. Khachonkham, S. Deycmar, C. Pessy, W. Dörr, P. Kuess, D. Georg, and S. Gruber. "Investigating the impact of α/β and LETd on relative biological effectiveness in scanned proton beams: An in vitro study based on human cell lines". In: *Med. Phys.* 47.11 (2020), pp. 5878–5888. DOI: 10.1002/mp.14470.

[40] N. Chumsuwan, P. Khongkow, S. Kaewsuwan, and K. Kanokwiroon. "Interruptin C, a Radioprotective Agent, Derived from Cyclosorus terminans Protect Normal Breast MCF-10A and Human Keratinocyte HaCaT Cells against Radiation-Induced Damage". In: *Molecules* 27.21 (2022), p. 7270. DOI: 10.3390/molecules27217270.

[41] Z. Zhang et al. "Heavy ion radiation induces pyroptosis in skin keratinocytes through a mitogen-activated protein kinase signaling pathway". In: *Int. J. Radiat. Biol.* 101.1 (2025), pp. 12–22. DOI: 10.1080/09553002.2024.2389401.

[42] S. Shakeri Manesh, T. Sangsuwan, A. Wojcik, and S. Haghdoost. "Studies of adaptive response and mutation induction in MCF-10A cells following exposure to chronic or acute ionizing radiation". In: *Mutat. Res. Genet. Toxicol. Environ. Mutagen.* 793 (2015), pp. 142–146. DOI: 10.1016/j.mrgentox.2015.06.012.

[43] Y.-F. Lin, H. Nagasawa, Y. Peng, E. Y. Chuang, and J. S. Bedford. "Comparison of Several Radiation Effects in Human MCF10A Mammary Epithelial Cells Cultured as 2D Monolayers or 3D Acinar Structures in Matrigel". In: *Radiat. Res.* 171.5 (2009), pp. 608–614. DOI: 10.1667/RR1598.1.

[44] V. Vandersickel, J. Slabbert, H. Thierens, and A. Vral. "Comparison of the colony formation and crystal violet cell proliferation assays to determine cellular radiosensitivity in a repair-deficient MCF10A cell line". In: *Radiat. Meas.* 46.12 (2011), pp. 1623–1628. DOI: 10.1016/j.radmeas.2011.05.006.

[45] L. Minafra et al. "Radiosensitizing effect of curcumin-loaded lipid nanoparticles in breast cancer cells". In: *Sci. Rep.* 9.1 (2019), p. 11134. DOI: 10.1038/s41598-019-47528-6.

[46] V. Bravatà et al. "Proton-irradiated breast cells: molecular points of view". In: *J. Radiat. Res.* 60.4 (2019), pp. 451–464. DOI: 10.1093/jrr/rrz029.

[47] R. L. Ramos, E. Bernardini, M. P. Carante, A. Ferrari, P. Sala, V. Vercesi, and F. Ballarini. "Radiation exposure of astronauts following an intense Solar Particle Event: analysis and comparison of doses in male and female voxel phantoms". In: *J. Radiol. Prot.* 44.4 (2024), p. 041508. DOI: 10.1088/1361-6498/ad7ff6.

List of Figures

List of Tables

Ringraziamenti

Al termine del lavoro di scrittura della tesi, è consuetudine rigraziare il relatore, il gruppo di lavoro e le persone grazie alle quale è stato possibile realizzare il progetto di tesi.
Ci tengo, invece, a precisare di non star ringraziando per consuetudine, ma per sincera gratitudine nei confronti di chi, con pazienza e attenzione, mi ha guidato in questi mesi di lavoro.
Primo tra tutti il mio relatore prof. Ricardo Luis Ramos per avermi accompagnato con cura e costanza in ogni fase del lavoro di tesi.
Ringrazio poi il prof. Mario Pietro Carante e la prof.ssa Francesca Ballarini per aver supervisionato il mio lavoro e dato consigli utili alla sua realizzazione.
Infine la dottoranda dott.ssa Alice Casali per essere stata disponibile e accogliente.
Oltre alle motivazioni puramente lavorative e didattiche, essenziali e impeccabili, però, vorrei ringraziare questo gruppo di lavoro per il clima disteso e di amicizia che ho respirato in questi mesi e che mi ha permesso di lavorare in maniera migliore e più rilassata. Nella mia piccola esperienza dei 5 anni universitari, so che è ben raro trovare un ambiente lavorativo in cui si trovino dei momenti per scherzare e per poter parlare anche di questioni personali. Sono stata piacevolmente sorpresa del fatto che, la mattina, all'arrivo in ufficio, alla domanda: "Come stai?" (domanda già di per sè non scontata) si rispondesse sinceramente su come si stava e non su quale tipo di lavoro di fosse fatto il giorno prima. Quindi grazie per avermi accolta nel vostro microcosmo.

Special thanks go to those who have accompanied me in my studies and throughout university over the past two years, and to those with whom I studied for exams and shared everyday student life, in no particular order: Bianca, Ric-

cardo, Silvia, Camila, Sina, Hannah, Amena, Rahamat, Elena, Giulia, and Nefeli. E poi un grazie di cuore a ciò che è stata casa per i passati due anni, ovvero il collegio Maria Ausialitrice (Maraus per gli amici :)) e a tutte le sue componenti, dalle suore, a ogni mia collegiale e amica. E un ringraziamento particolare al Piedibus (Chiara A., Chiara M., Fede, Elena, Vale) e Anna G. non può mancare. Questi due anni non sarebbero potuti essere altrettanto sereni se non avessi avuto così tanto sostegno anche a Torino. In primis dai miei genitori, dalle mie sorelle, dalla nonna Maria e dalla mia famiglia tutta. Come non citare poi Broccolo (Marghe, Paola, Viola, Maria, Giulia e Gioana), Maria Giulia e, infine, Federico. Grazie per esserci stati.